#### **Review Article**

Jie Wu, Xuqi Yang, Jing Chen, Shiyu Li, Tianchen Zhou, Zhikuang Cai\*, Xiaojuan Lian\*, and Lei Wang\*

# Overview of amorphous carbon memristor device, modeling, and applications for neuromorphic computing

https://doi.org/10.1515/ntrev-2023-0181 received August 22, 2023; accepted December 11, 2023

Abstract: Carbon-based materials strongly pertain to citizens' daily life due to their versatile derivatives such as diamond, graphite, fullerenes, carbon nanotube, singlelayer graphene, and amorphous carbon (a-C). Compared to other families, a-C exhibits reconfigurable electrical properties by triggering its sp<sup>2</sup>-sp<sup>3</sup> transition and vice versa, which can be readily fabricated by conventional film deposition technologies. For above reasons, a-C has been adopted as a promising memristive material and has given birth to several physical and theoretical prototypes. To further help researchers comprehend the physics behind a-C-based memristors and push forward their development, here we first reviewed the classification of a-C-based materials associated with their respective electrical and thermal properties. Subsequently, several a-C -based memristors with different architectures were presented, followed by their respective memristive principles. We also elucidated the state-of-the-art modeling strategies of a-C memristors, and their practical applications on neuromorphic fields were also described. The possible scenarios to further mitigate the physical performances of a-C memristors were eventually discussed, and their future prospect to rival with other memristors was also envisioned.

**Keywords:** amorphous carbon, memristor, neuromorphic, model, device

#### 1 Introduction

Carbon-based materials have been considered as one of the most prospective contenders for conventional silicon (Si)-based semiconductors [1,2]. This can be ascribed to its abundant sources, superior performances and good environmental compatibility. In addition to the well-known diamond and graphite, several attractive derivatives of carbon-based materials, such as fullerenes, carbon nanotube (CNT), single-layer graphene, and amorphous carbon (a-C), have been discovered in the past [3–6], as revealed from Figure 1. Such versatility endows carbon-based materials with excellent mechanical, electrical, and optical properties, thus making them suitable for various electronic components that include transistors [7], sensors, field emission device [8], and anti-radiative devices [9].

In addition to the above applications, carbon-based materials have recently been adopted as a promising candidate for emerging memristor technologies. According to the classic definition [10], memristor, usually nominated as the fourth fundamental element of the circuit, is a twoterminal device whose resistance can be switched between high resistive state (HRS) and low resistive state (LRS) via external stimulus [10]. Most importantly, such resistance modulation process is usually accompanied with several physical superiorities such as high switching speed, long endurance, good retention, and low power consumption [11]. Additionally, its fairly simple architecture considerably shrinks the occupied area, and consequently booms resulting density [12]. These remarkable merits make memristor completely resemble synapses and neurons of biological brain, and open a new path towards neuromorphic applications [13]. As illustrated in Figure 2, the mainstream

**Jie Wu, Xuqi Yang, Jing Chen, Shiyu Li, Tianchen Zhou:** College of Integrated Circuits Science and Engineering, Nanjing University of Posts and Telecommunications, No. 9 Wenyuan Road, Nanjing 210023, Jiangsu, China

<sup>\*</sup> Corresponding author: Zhikuang Cai, College of Integrated Circuits Science and Engineering, Nanjing University of Posts and Telecommunications, No. 9 Wenyuan Road, Nanjing 210023, Jiangsu, China, e-mail: whczk@njupt.edu.cn

<sup>\*</sup> Corresponding author: Xiaojuan Lian, College of Integrated Circuits Science and Engineering, Nanjing University of Posts and Telecommunications, No. 9 Wenyuan Road, Nanjing 210023, Jiangsu, China, e-mail: xjlian@njupt.edu.cn

<sup>\*</sup> Corresponding author: Lei Wang, College of Integrated Circuits Science and Engineering, Nanjing University of Posts and Telecommunications, No. 9 Wenyuan Road, Nanjing 210023, Jiangsu, China, e-mail: leiwang1980@njupt.edu.cn

— Jie Wu et al. DE GRUYTER

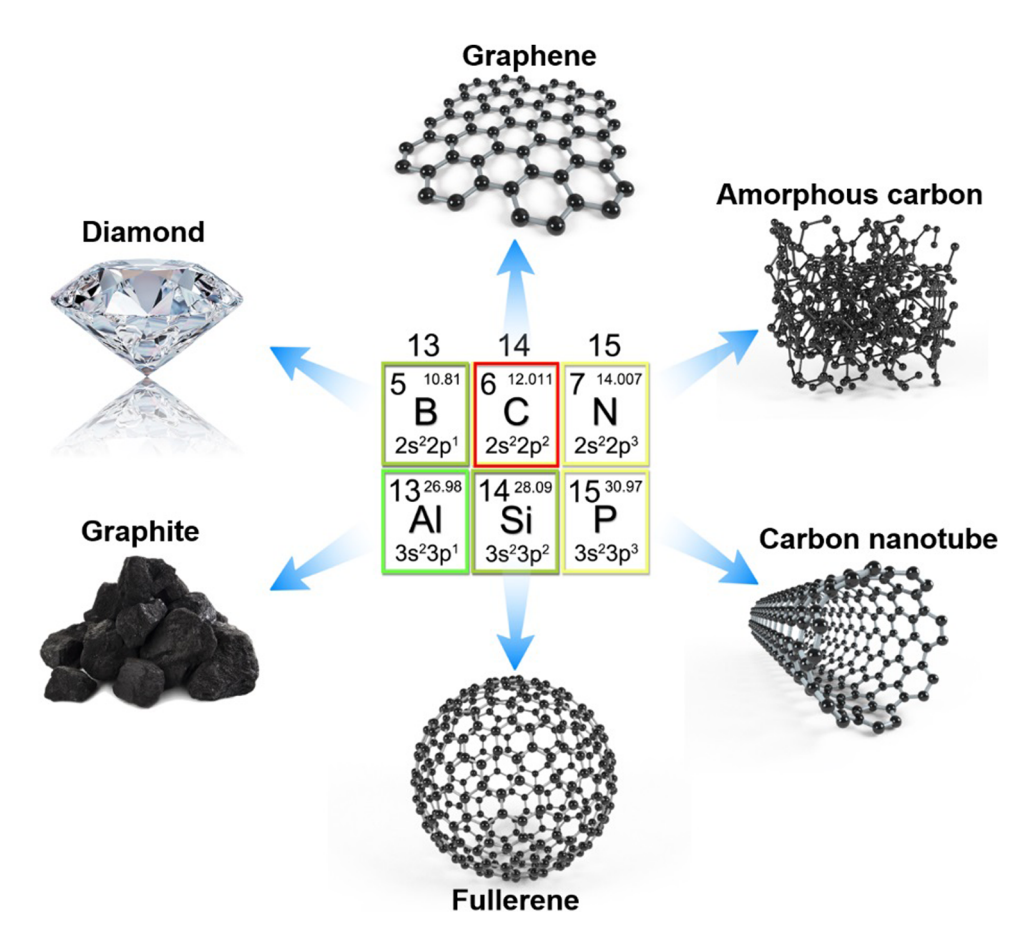


Figure 1: Appearances of the most studied carbon allotropes today.

memristive materials today include transition metal oxides (TMOs) [14,15], chalcogenides [16,17], ferroelectric materials [18,19], and magnetic materials [20,21]. In comparison with these well studied materials, aforementioned carbon derivatives also exhibited resistive switching (RS) behaviors when subjected to stimulus. More excitingly, their inherent physical properties assigned carbon-based memristors with some fascinating traits such as low toxicity, chemical stability, and flexibility over conventional memristive materials [22]. Within various carbon derivatives, a-C-based memristor has been receiving consistent attention during the last decade, owing to their flexibility on RS and mature fabrication techniques. This led to the birth of multiple a-C-based device prototypes and modeling algorithms. Nevertheless, a comprehensive review on the state-of-the-art a-C-based memristor technologies is still missing from the perspective of either device physics or theoretical simulations. It is therefore necessary to provide a comprehensive overview of different types of a-C-based memristors, including their material composition, operating principles and performance characteristics, whereby researchers can better understand the diversity and potential application areas of a-C-based memristors through such systematic summarization. To address this drawback, here we

first reviewed the classification of a-C-based materials associated with their respective electrical and thermal properties. Subsequently, several a-C-based memristors with different architectures were presented, followed by their respective memristive principles. We also elucidated the state-of-the-art modeling strategies of a-C memristors, and their practical applications on neuromorphic fields were also described. The possible scenarios to further mitigate the physical performances of a-C memristors were eventually discussed, and their future prospect to rival with other memristors was also envisioned. The aim of the article is to provide a comprehensive overview of different types of a-C-based memristors, including their material composition, operating principles, and performance characteristics. Through the systematic summarization, readers can better understand the diversity and potential application areas of a-C-based memristors.

#### 2 a-C classification

a-C families can be physically discriminated via the following critical features: (1) the  $sp^3$  content, (2) the

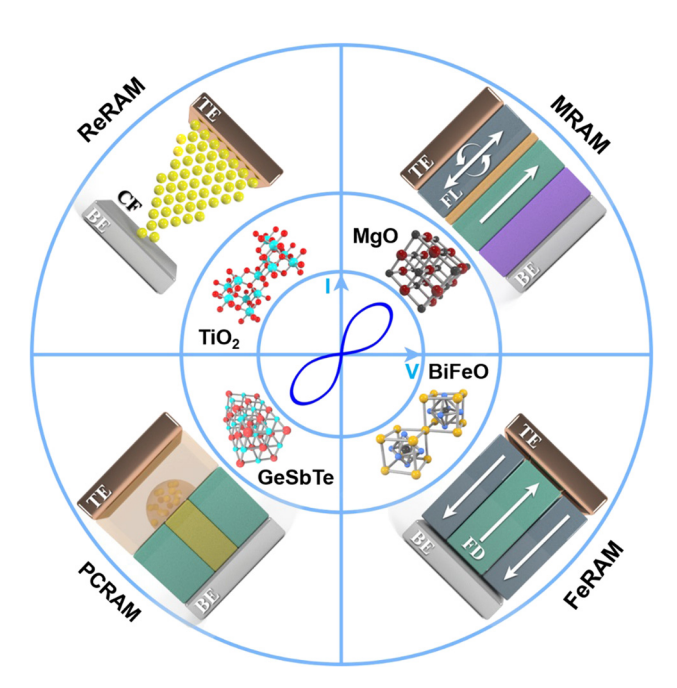


Figure 2: Common memristive materials and their corresponding memristor devices. The inner most ring exhibits the typical I-V characteristic of memristor, described visually as a pinched hysteresis loop. The middle ring presents common memristive materials that can be represented clockwise as MgO, BiFeO, GeSbTe, and TiO2, respectively. The outer most ring in clockwise shows their corresponding memristors, classified into magnetic random access memory (MRAM), Ferroelectric RAM (FeRAM), phase-change RAM (PCRAM), and resistive RAM (ReRAM).

clustering of the sp<sup>2</sup> phase, (3) the orientation of the sp<sup>2</sup> phase, (4) the cross-sectional nanostructure, and (5) the hydrogen (H) or nitrogen (N) content [23], as clearly illustrated in Figure 3 in the form of ternary phase diagram. Note that the structure versatility of carbon materials mainly arises from their different bonding hybridizations, i.e., sp<sup>3</sup>, sp<sup>2</sup>, and sp<sup>1</sup>. sp<sup>3</sup> hybridization indicates a carbon atom  $\sigma$  bonded to four other atoms, resulting in a mixture of one s orbital and three p orbitals in the same shell of an atom to form four new equivalent orbitals. sp<sup>2</sup> hybridization corresponds to a formation of two single  $\sigma$  bonds and one double  $\sigma$  bond among three atoms, revealing a mixture of one s orbital and two p orbitals in the same shell of an atom to form three equivalent orbitals. Carbon having sp hybridization is bounded to two other atoms through a combination of either two double bonds or one single and two triple bonds, making a mixture of one s orbital and one p orbital in the same shell of an atom to form two new equivalent orbitals. Three corners of the triangle in Figure 3 correspond to graphite, diamond, and hydrocarbons, respectively. Carbon ordering along the graphite-diamond line can be classified into graphite, nanocrystalline graphite, sp<sup>2</sup>-dominated a-C, sp<sup>3</sup>-dominated a-C, and diamond [23–25]. Such ordering variations, involving sp<sup>2</sup> clustering

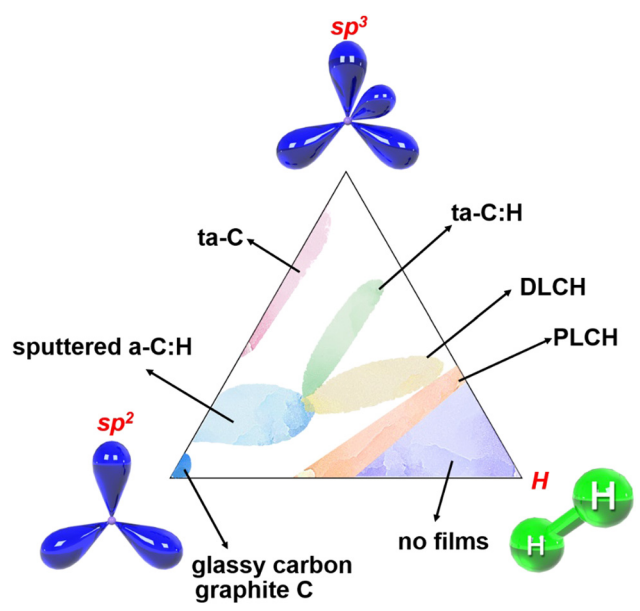


Figure 3: A ternary phase diagram for a-C.

evolution and sp<sup>3</sup> content evolution, can result from different deposition techniques. Note that one of the most important carbon ordering phases along the graphite-diamond line is tetrahedral a-C (i.e., ta-C) with maximum sp<sup>3</sup> content. The key technique to deposit ta-C film is ion bombardment, which can be realized by pulsed laser deposition, filtered cathodic vacuum arc, and mass-selected ion beam deposition [26-29]. High proportion of sp<sup>3</sup> hybridization endows ta-C with various attractive properties such as high elastic modulus, chemical inertness, high hardness, high electrical resistivity, and optical transparency, thus attaining considerable attention for electro-optical applications [30–32].

In addition to hydrogen-free a-C, hydrogenated a-C alloy (a-C:H) is also one of the most researched materials owing to its novel optical, mechanical, and electrical properties and its similarities to diamond. It was reportedly classified into four groups. The first group is the a-C:H having 40–60% H content with up to 70% sp<sup>3</sup>. The materials inside this group are soft and has low density [6], usually referring to polymer-like a-C:H (PLCH). The second a-C:H group is defined to have 20-40% H content. Such group exhibits more excellent mechanical properties because of more C-C sp3 bonds [6]. These films are usually called diamond-like a-C:H (DLCH). Increasing the sp<sup>3</sup> content (~70%) of DLCH resulted in ta-C:H with larger optical gap and higher density [33]. The last group a-C:H has low H content (≤20%), corresponding to higher sp<sup>2</sup> content and sp<sup>2</sup> clustering. These films are usually named as graphitelike a-C:H (GLCH). Plasma enhanced chemical vapor deposition (PECVD) has been considered as the most common approach to deposit a-C:H films such as PLCH [34,35],

DLCH [35,36], and GLCH [35,36], while ta-C:H films can be deposited by electron cyclotron wave resonance [37] and plasma beam source techniques [38].

Another important type of a-C is carbon nitrides that can also be categorized into four classes. The first class of carbon nitrides is a-C:N with a high sp<sup>2</sup> bonds content, which is required to be deposited above 200°C and allows for better mechanical hardness and large elastic recovery [39.40], ta-C:N is usually defined to be the second class of carbon nitrides, which presents smaller resistivity and optical gap than pure ta-C films [41]. Note that ta-C:N exhibits high sp<sup>3</sup> content (80-90%) up to about 10% N, after which its sp<sup>3</sup> content and density decrease sharply [41]. Such trend was ascribed to the high deposition pressure [42]. Implementing PECVD using a mixture of a hydrocarbon gas enables the deposition of a-C:H:N [43,44], regarded as the third class of carbon nitrides. Increasing N content can however reduce the hardness of a-C:H:N films, and a more graphite-like material can be obtained by decreasing the N and H contents [41]. ta-C:H:N, the last class of carbon nitrides, is usually secured by introducing N into ta-C:H, which gives rise to sp<sup>2</sup> clustering and maintains an inappreciable sp $^3$  to sp $^2$  conversion within  $\sim 20\%$ N content. Increasing N contents can result in lower sp<sup>3</sup> fraction and softer films [45].

### 3 Modeling of a-C-based memristor

The concept of the a-C-based memristor originated from the finding of RS phenomenon on a so-called "insulation" carbon film sandwiched between a bottom tungsten (W) electrode and a top metal electrode. It was postulated that the initial form of the carbon material is a diamond structure dominated by sp³ with low conductivity. After applying voltage to the metal electrodes at both ends, part of sp³ is transformed into a graphite structure dominated by sp² with high conductivity under the action of high current density, forming a conductive filament connecting the upper and lower electrodes. Under the influence of the high current density, the thin metal electrode melts, and the fine carbon filaments are oxidized and evaporated, thus forming the fine filamentous crater [46], as illustrated in Figure 4(a).

Following such hypothesis, majority of a-C memristor models were devoted to the imitation of sp<sup>2</sup>-to-sp<sup>3</sup> conversion and *vice versa* [47–51]. One reported work defined the resistance switching behavior as the well-known "threshold switching," which can be described by a modified Poole–Frenkel (P-F) type conduction [47]:

$$I = K'e^{\left[-\frac{\Phi_{\rm B}}{k_{\rm B}T}\right]} \sinh\left[\frac{q}{k_{\rm B}T}\frac{V\,\mathrm{d}z}{2t}\right],\tag{1}$$

where K' is a constant and  $\Phi_B$ ,  $k_B$ , T, q, and t are the energy barrier at zero field, Boltzmann constant, temperature, elementary charge, and thickness of the film, respectively. dz is the average inter-trap distance. LRS according to the P-F model occurs by the field assisted thermionic emission of electrons from donor traps lying just below the conduction band edge, while HRS was dominated by the hopping conduction via states near the Fermi level within the mobility gap [52]. It was further speculated that the induced electric field increased the sp<sup>2</sup> clusters in size and caused reversible bond rearrangements [53]. This subsequently reduced the inter-trap distance, and lowered the effective barrier height from HRS to LRS, thus contributing to the remarkable reduction in electrical resistance. The experimental current-voltage (I-V) curve and the corresponding fit agreed well, as reflected in Figure 4(b). Another hypothesis ascribed RS behaviors to the gradual decrease in the height of formed potential barrier within the device [53]. As illustrated in Figure 4(c), it was observed that HRS and LRS I-V characteristics were consistent with current transport by direct tunneling through a barrier at low voltages, followed by Schottky emission over a barrier at high voltages. The barrier heights, depending on the structural rearrangements, gradually decreased, thus giving rise to different resistance states. Instead of directly deriving the sub-threshold current, an alternative strategy was to define the electrical conductivities of the a-C at subthreshold  $(\sigma_{LF})$  and threshold switching  $(\sigma_{HF})$  regimes, respectively, given by [48]:

$$\sigma_{\rm LE} = \frac{K_{\rm LE}T}{E} e^{\frac{-E_a}{k_{\rm B}T}} \sinh\left(\frac{eEs}{2k_{\rm B}T}\right),\tag{2}$$

$$\sigma_{\rm HE} \approx \frac{K_{\rm LE}T}{E^{\frac{1}{2}}} \left[ 1 - \frac{k_{\rm B}T}{\beta E^{\frac{1}{2}}} \right] e^{-\left[\frac{E_{\rm a} - \beta E^{\frac{1}{2}} + \frac{\beta^2}{e_{\rm S}}}{k_{\rm B}T}\right]},$$
(3)

where  $K_{\rm LE}$  and  $K_{\rm HE}$  are prefactors for  $\sigma_{\rm LE}$  and  $\sigma_{\rm HE}$ , respectively, E is the electric field,  $E_{\rm a}$  is the low-field temperature dependent activation energy, s is the distance between two coulombic centers,  $\beta$  is the Pool–Frenkel constant. Accordingly, the electrical conductivity of the a-C was assumed to be  $\sigma_{\rm LE}$  when the electric field was smaller than a pre-defined threshold value, while it was considered as  $\sigma_{\rm HE}$  when resulting electric field exceeded the threshold value. Resulting electrical conductivities from above definitions also matched the experimentally measured case well, as shown in Figure 4(c). Differing from the above two methods, another scenario to mimic the RS of a-C

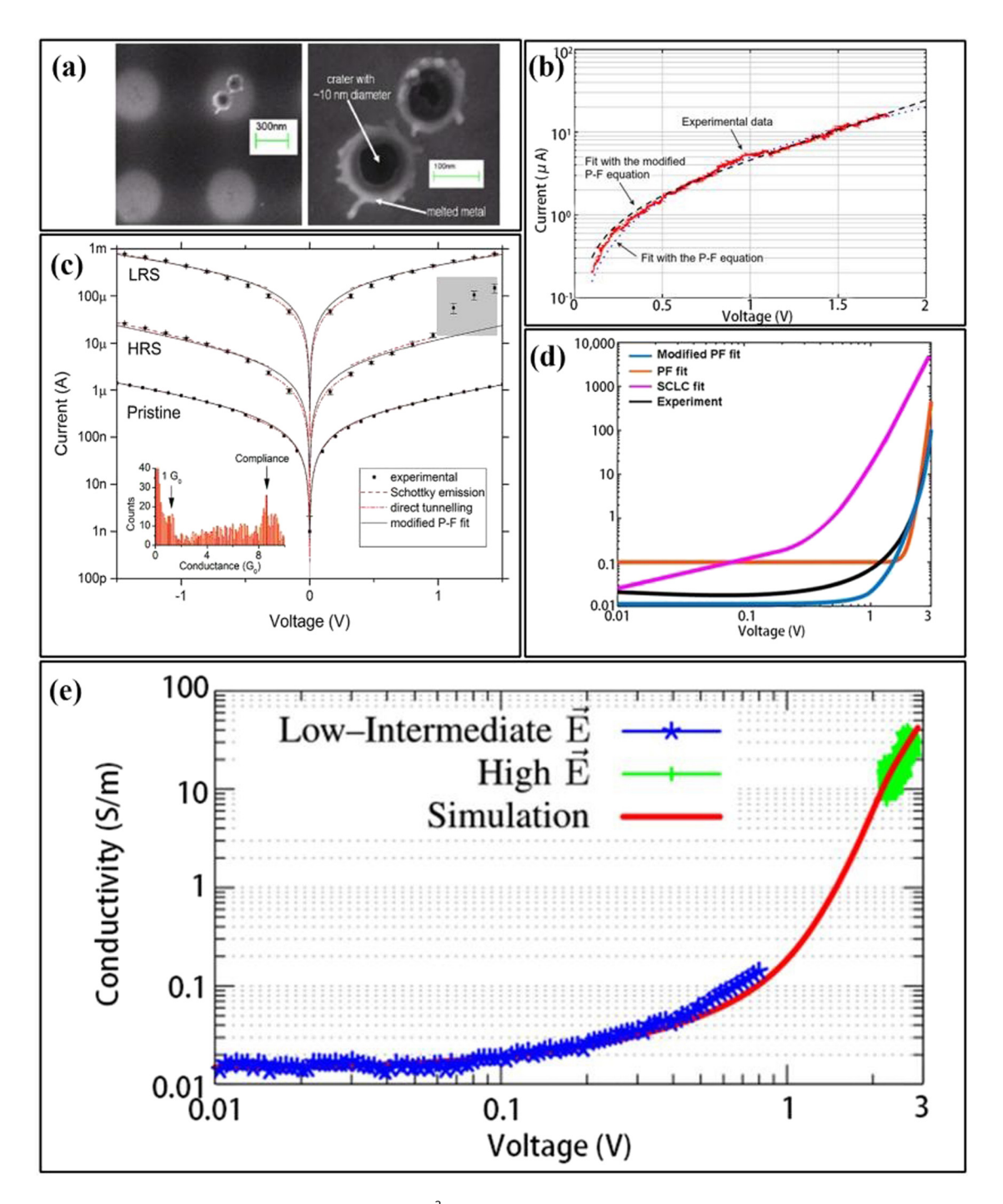


**Figure 4:** (a) Two spots formed inside the melted metal where sp<sup>2</sup> filaments were oxidized and vaporized, leaving two craters (left) and their zoom-in image (right), (b) simulated and measured I–V curves of a TiN/a-C/PtSi conductive tip stack, resulting from the modified Poole–Frenkel model, (c) experimental data of the device in its three states. Included are theoretical fits for a barrier (direct tunnelling and Schottky emission) model and a modified P-F model, (d) simulated electrical conductivity of a-C sandwiched between TiN and PtSi conductive tip, based on different physical assumptions, and (e) comparison between measured and calculated electric field-dependent electrical conductivities of an a-C-based device (Pt/ta-C/W). (a), (b), (c), and (d) are reprinted with permission from [46–49], respectively.

was to define the electrical conductivities of  $sp^2$  and  $sp^3$  contents, respectively. The electrical conductivity of  $sp^2$  content was regarded as a constant of  $1.2 \times 10^5 \ \Omega^{-1} \ m^{-1}$ , while that of  $sp^3$  content was interpreted as [49]:

$$\sigma_{\rm sp^3} = 0.345 \cdot e^{-\frac{220}{T^{1/4}}} \cdot \sinh\left(\frac{E}{9.5 \cdot 10^9}\right) + 0.0115.$$
 (4)

The electrical conductivities of the a-C-based carbon memory device for different bias voltages were therefore 6 — Jie Wu *et al.* DE GRUYTER

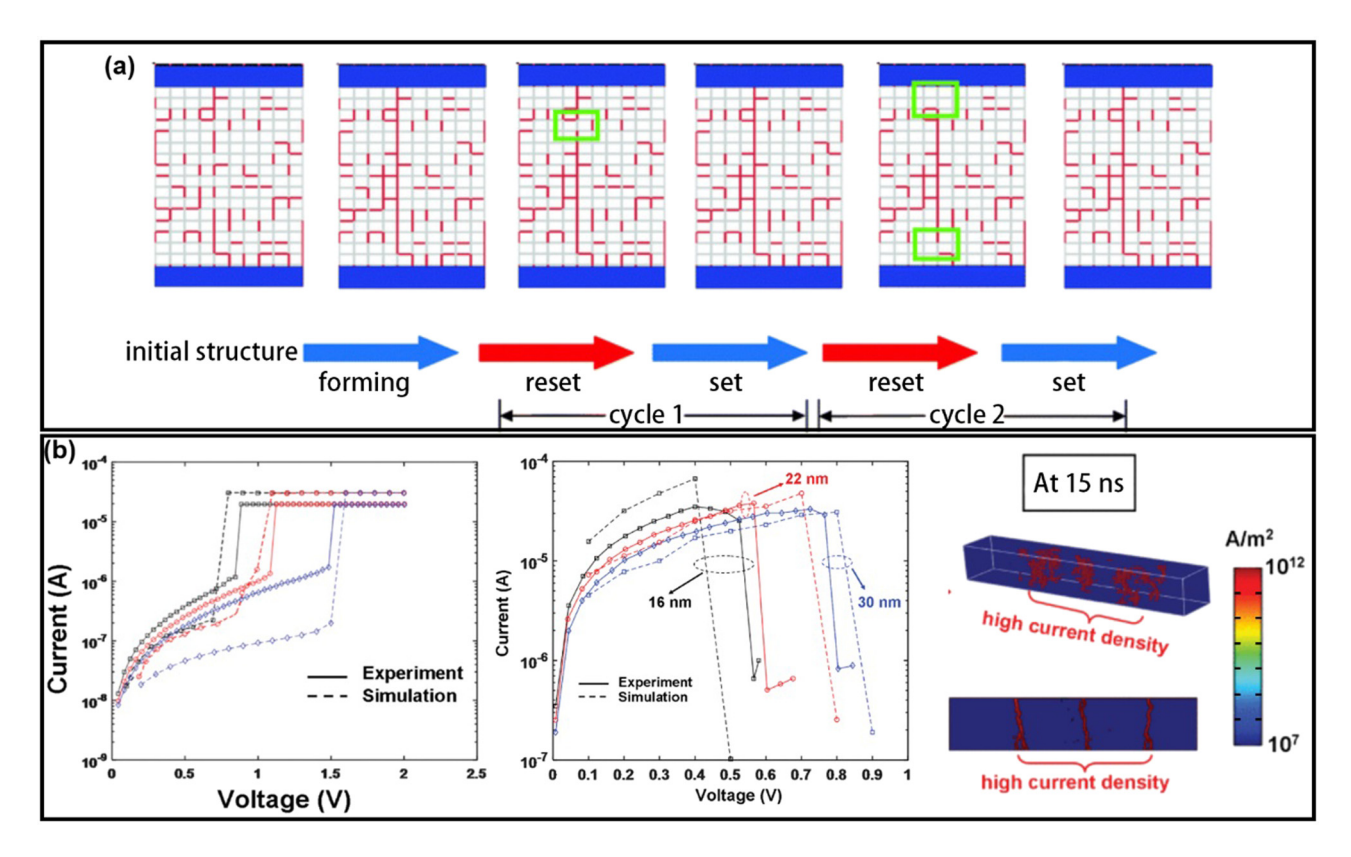


**Figure 5:** (a) Formation and breakage of conductive a-C filaments inside an a-C-based device for two successive cycles. Green rectangles indicate the locations where the breakage of a-C filaments occurred. (b) Measured and calculated "SET" (left) and "RESET" (middle) current for different a-C thicknesses, and simulated current density (right) inside the a-C layer. (a) and (b) are reprinted with permission from [50,51], respectively.

calculated and found to show a good agreement with the measured values, as demonstrated in Figure 4(d).

It should be kept in mind that for the above models, physical conversions between  $sp^2$  and  $sp^3$  contents were only described in terms of device resistances. This implied that aforementioned models were unable to predict the exact proportions of  $sp^2$  and  $sp^3$  contents. To address this issue, mass action law was combined with the electrothermal model to determine the concentrations of  $sp^2$  and  $sp^3$  contents, constructed by [50]:

$$\frac{\mathrm{d}r_{\rm sp^2}}{\mathrm{d}t} = -k_f r_{\rm sp^2} + k_r (1 - r_{\rm sp^2}),\tag{5}$$

where  $r_{\rm sp^2}$  is the concentration of  ${\rm sp^2}$  content, t is the time,  $k_f$  and  $k_r$  correspond to the reaction rates for the transition from  ${\rm sp^2}$  to  ${\rm sp^3}$  and  ${\rm sp^3}$  to  ${\rm sp^2}$ , respectively. The reaction rate  $k_r$ , governing "SET" operation (i.e.,  ${\rm sp^3}$  to  ${\rm sp^2}$ ), was attributed to the outcome of the electric field intensity, defined by

$$k_r = \begin{cases} k_{r_0} \frac{|E| - |E_0|}{E_0}, & |E| > |E_0|, \\ 0, & |E| < |E_0|, \end{cases}$$
 (6)

where  $|E_0|$  and  $k_{r_0}$  are the fitting parameters in describing the threshold of the electrical field intensity and reaction rate constant from sp<sup>3</sup> to sp<sup>2</sup>, respectively. In contrast, the reaction rate  $k_f$ , responsible for "RESET" operation (*i.e.*, sp<sup>2</sup> to sp<sup>3</sup>), was liable to be dominated by non-uniform temperature distribution, calculated by

$$k_f = \begin{cases} k_{f_0} \frac{|\nabla T| - |\nabla T|_0}{|\nabla T|_0}, & |\nabla T| > |\nabla T|_0, \\ 0, & |\nabla T| < |\nabla T|_0, \end{cases}$$
(7)

where  $|\nabla T|_0$  and  $k_{f_0}$  are the fitting parameters in describing the threshold of the temperature gradient intensity and reaction rate constant from  $\mathrm{sp^2}$  to  $\mathrm{sp^3}$ , respectively. By simultaneously solving above mass diffusion model with electro-thermal model, it was possible to dynamically reproduce the formation and rupture of the conductive filaments (CFs) inside the a-C layer, and thus to determine the volume fractions of the  $\mathrm{sp^2}$  and  $\mathrm{sp^3}$  contents, as demonstrated in Figure 5(a). As can be seen from Figure 5(a), the a-C precursor film consisted of numerous breakers that were adopted to describe the path between two neighboring spots, which can be defined as either  $\mathrm{sp^2}$ 

(red) or sp³ (grey) clusters. It was clearly observed that during the "RESET" process, the red breakers inside the green box were missing, corresponding to the rupture of the CFs. In contrast, previous gaps between different spots were re-connected by red breakers, implying the formation of new CFs. One severe drawback of the above model arose from the fact that it did not take into account the complex electrical transport mechanism of a-C films. As a result, another model that included both electrical transport behaviors of a-C films with the reaction rates of sp² to sp³ and sp³ to sp² conversions has recently been proposed [51,54]. The electrical transport behaviors of a-C films were elaborated based on equations (2) and (3), while reaction rates slightly differed from equations (6) and (7), resulting in

$$k_{\rm sp^3 \to sp^2} = c_1 e^{-\frac{E_a - \beta E^{\frac{1}{2}} + \frac{\beta^2}{6S}}{k_B T}},$$
 (8

$$k_{\rm sp^2 \to sp^3} = c_2 e^{-\frac{E_b}{k_{\rm B}T}},$$
 (9)

where  $c_1$  and  $c_2$  denote different prefactors for sp<sup>2</sup> to sp<sup>3</sup> and sp<sup>3</sup> to sp<sup>2</sup> conversions, respectively, and  $E_b$  represents the activation energy for sp<sup>2</sup> to sp<sup>3</sup> conversion. By means of this comprehensive model, the "SET" current was calculated and promisingly coincided with the experimental counterpart. More importantly, such approach allowed for the visualization of the conductive filament formation and erasure in three-dimension (3D), as illustrated in Figure 5(b), which can be employed to predict the threshold switching voltages for a variety of preliminary sp<sup>2</sup> fractions. Note that few researchers [50,51,54] considered the transition from LRS to HRS as the sole temperature-dependent rehybridization of sp<sup>2</sup> atoms to sp<sup>3</sup> atoms, which generated separations in the conductive bridge through the a-C layer or the contact regions. However, as the sp<sup>2</sup> phases of carbon are thermodynamically favored at atmospheric pressure, the speculation that the transition from LRS to HRS only relied on temperature remained doubtful. Qin et al. [50]

also proposed that resulting pressures from temperature gradient may facilitate the presence of HRS by driving sp<sup>2</sup> atoms to sp<sup>3</sup> atoms owing to thermal expansion, whereas experimental evidences that pressures were required to form sp<sup>3</sup> phase were still missing.

Table 1 summarizes the working mechanisms of various a-C-based memristor models reported so far.

## 4 Design principles of a-C-based memristors

According to the reported modeling results, one viable approach to achieve its memristive character is to change the ratio of sp<sup>2</sup> to sp<sup>3</sup> bond either electrically or thermally. Besides, the electrochemical metallization of the CFs for conventional ReRAMs using TMOs also applies to a-C-based memristor by appropriately choosing the capping metal electrode. Moreover, doping a-C with other reactive elements can also tailor the electrical properties of a-C effectively. For above reasons, a-C-based memristor here is simply classified into undoped a-C-based memristor and doped a-C-based memristor.

#### 4.1 Undoped a-C-based memristor

Various architectures of undoped a-C-based memristors have previously been proposed by several groups [55–64]. Despite these architecture variations, majority of these memristors shared one common configuration, *i.e.*, top metal electrode/a-C/bottom metal electrode structure. The top electrode in fact plays a more important role in determining the RS mechanism of the undoped a-C-based memristor than the bottom electrode. The a-C-based memristor whose top electrode is made of active metal, such as silver (Ag), copper (Cu),

Table 1: Characteristic parameters of different a-C memristor models

Structure	Electrical switching	$sp^2 \Leftrightarrow sp^3$ switching	Ref.
TiN/a-C/C-AFM tip	Modified Poole–Frenkel	_	[47]
TiN/ta-C/C-AFM tip	Modified Poole-Frenkel	_	[48]
Graphitic-C/a-C/graphitic-C	Modified Poole-Frenkel	Electric field-dependent	[53]
Pt/ta-C/W	$sp^2$ : constant $\sigma$	_	[49]
	${\sf sp^3}$ : field and temperature dependent $\sigma$		
Bottom/a-C/top	Poole–Frenkel tunneling	Mass action law	[50]
TiN/a-C/Pt	Modified Poole-Frenkel	Rate law	[51]
TiN/ta-C/C-AFM tip	Modified Poole-Frenkel	Rate law	[54]

and gold (Au), usually exhibits a bipolar switching characteristic such that modulation of resistive states is realized by alternating the polarity of the applied bias, as reflected in Figure 6(a).

Similar to the widely studied TMO memristors, such bipolar switching commonly results from the formation and rupture of conductive bridges *via* the diffusion of dissolved metal cations from the interface of the electro-chemically active electrode into the a-C region and *vice versa* [65,66]. The metal cations, stemming from the oxidization of the electrochemically active metals, can migrate into the a-C layer to form conductive channels, driven by the positive electric field. Since a-C films reportedly exhibited low ion mobility and redox rates [67], metal cations were able to accumulate and reach the critical nucleation conditions inside the a-C layer under high field bias. Moreover, the local electric field near the conductive sp<sup>2</sup> sites can be significantly

enhanced due to the dielectric mismatch between the sp<sup>2</sup> and sp<sup>3</sup> sites [68], thus making these sp<sup>2</sup> atoms as nucleation sites. The advent of enhanced electrical field undoubtedly increased the nucleation probability of metal cations and improved nucleation process. In contrast, a negative voltage applied to active electrode can induce oxidation and potential Joule heating effect, which facilitates the dissolution of previously formed conductive channels. According to the above mechanism, both non-volatile and volatile RS behaviors were found on one memristor configuration based on Cu/a-C/Pt design [59]. It was reported that changing CCs can vary the size of CFs, thus giving rise to different RS types. One simple method to further mitigate the RS performance of the Cu/a-C/Pt structure was implemented to adjust the degree of sp<sup>2</sup> clustering by changing CCs, as shown in Figure 6(b) [56]. The small sp<sup>2</sup> clusters can gather to become larger clusters along with increasing CCs, and conductive

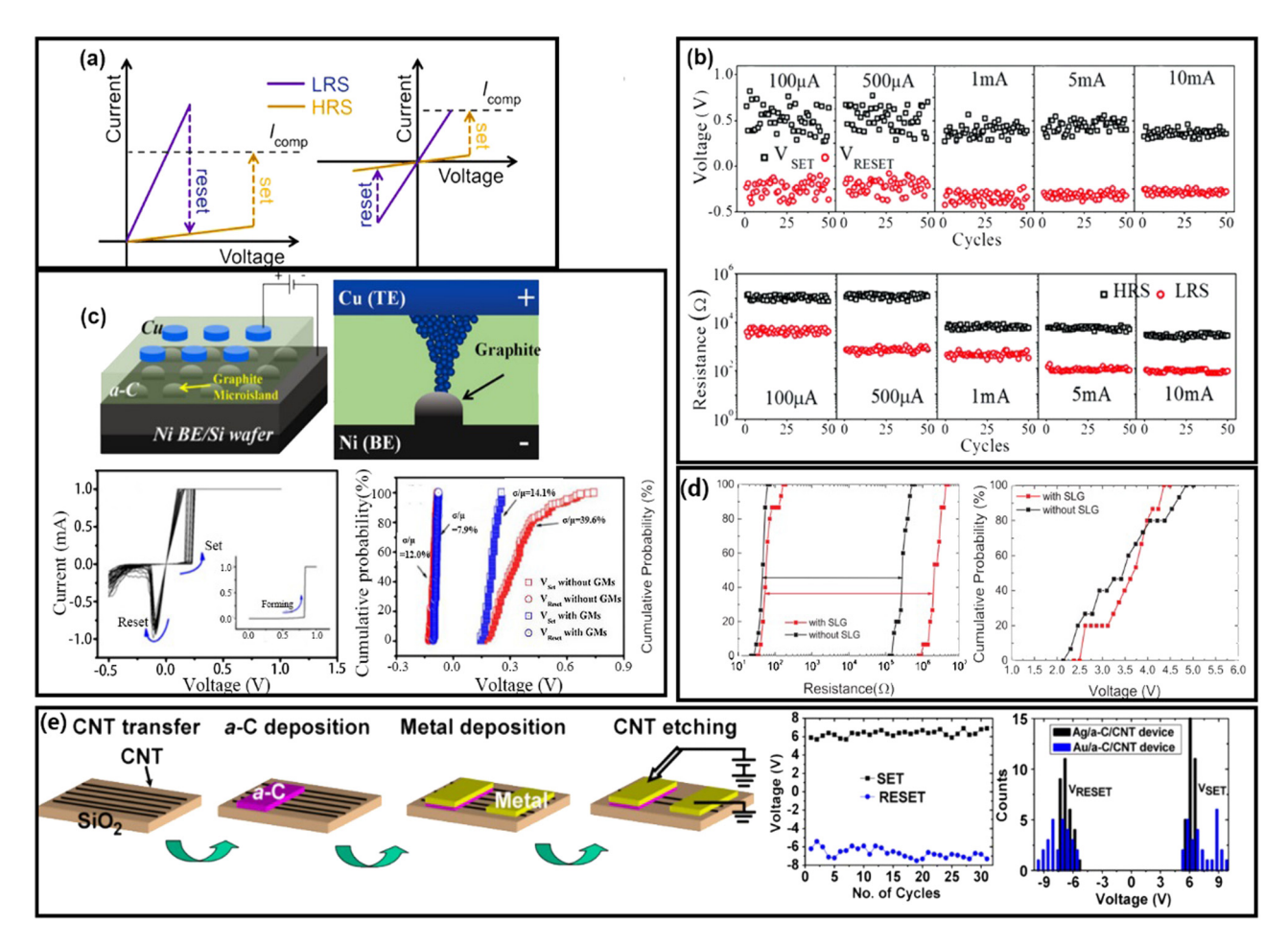


**Figure 6:** (a) Unipolar (left) and bipolar (right) switching I–V curves, (b) SET/RESET voltages (top) and HRS/LRS (bottom) distributions for different compliance currents (CCs), (c) schematic of a-C memristor embedded with graphite microislands (GMs) (top) and its resulting I–V curves (bottom), (d) the cumulative probability of HRS/LRS (left) and operation voltage (bottom) with and without single-layered graphite (SLG), (e) fabrication process of the metal/a-C/CNT/metal memory (left), and SET/RESET voltages distribution during different programming cycles and statistical distribution of SET/RESET voltages for different metal electrodes (*i.e.*, Au and Aq). (b), (c), (d), and (e) were reprinted with permission from [55–57,64], respectively.

channels can be produced along the pre-formed sp<sup>2</sup> clusters, thus improving the memristor performance. This method has recently been improved by producing uniform GMs inside the Cu/a-C/nickel (Ni) memristor [64], as illustrated in Figure 6(c). The conductive filaments were apt to grow along the GMs, and the enhanced local electric field around the GMs not only reduced the energy consumption, but also suppressed the relative fluctuation of HRS/LRS resistance. In addition to the optimization of a-C film itself, physical performances of undoped a-C-based memristor can also be alleviated by utilizing different electrode materials. One paradigm is to insert an additional SLG between top Au electrode and ta-C film to form Au/SLG/ta-C/Pt structure [55], as shown in Figure 6(d). This novel configuration allowed for both bipolar switching and unipolar switching, while inducing ten times higher ON/OFF ratio than the sole metal electrode. This was likely caused by a suppressed tunneling current due to the low density of states of graphene near the Dirac point [55]. Another device that adopted Au/a-C/CNT architecture was also studied (Figure 6(e)), substantially reducing the size of the active device area [57].

Another type of undoped a-C-based memristor is accompanied with top inert electrode such as platinum (Pt), tungsten (W), and chromium (Cr). Unipolar switching was reportedly the main RS behavior of the a-C memristor with top inert electrode [57]. This is because the generated CF inside the a-C film that governs its RS behavior is only made of sp<sup>2</sup> carbon bond. As bipolar switching is more controllable than unipolar switching [57], undoped a-C-based memristor with inert top electrode has received less attention than that with active electrode. One typical architecture was Pt/a-C/W memristor [60], as shown in Figure 7(a). Such memristive characteristic, arising from the formation and rupture of conductive graphitic filaments, exhibited several merits such as high ON/OFF resistance ratio, high switching speed, low operation voltage, low power consumption, and good reliability. Similar results were also observed on the same Pt/a-C/W memristor configuration by different groups, leading to good scaling-down properties (Figure 7(b)) [58]. To further improve the memristor performances, it was possible to sputter the a-C target with argon and ammonia (NH<sub>3</sub>) gas [62], resulting in Pt/C(NH<sub>3</sub>)/TiN memristor (Figure 7(c)).

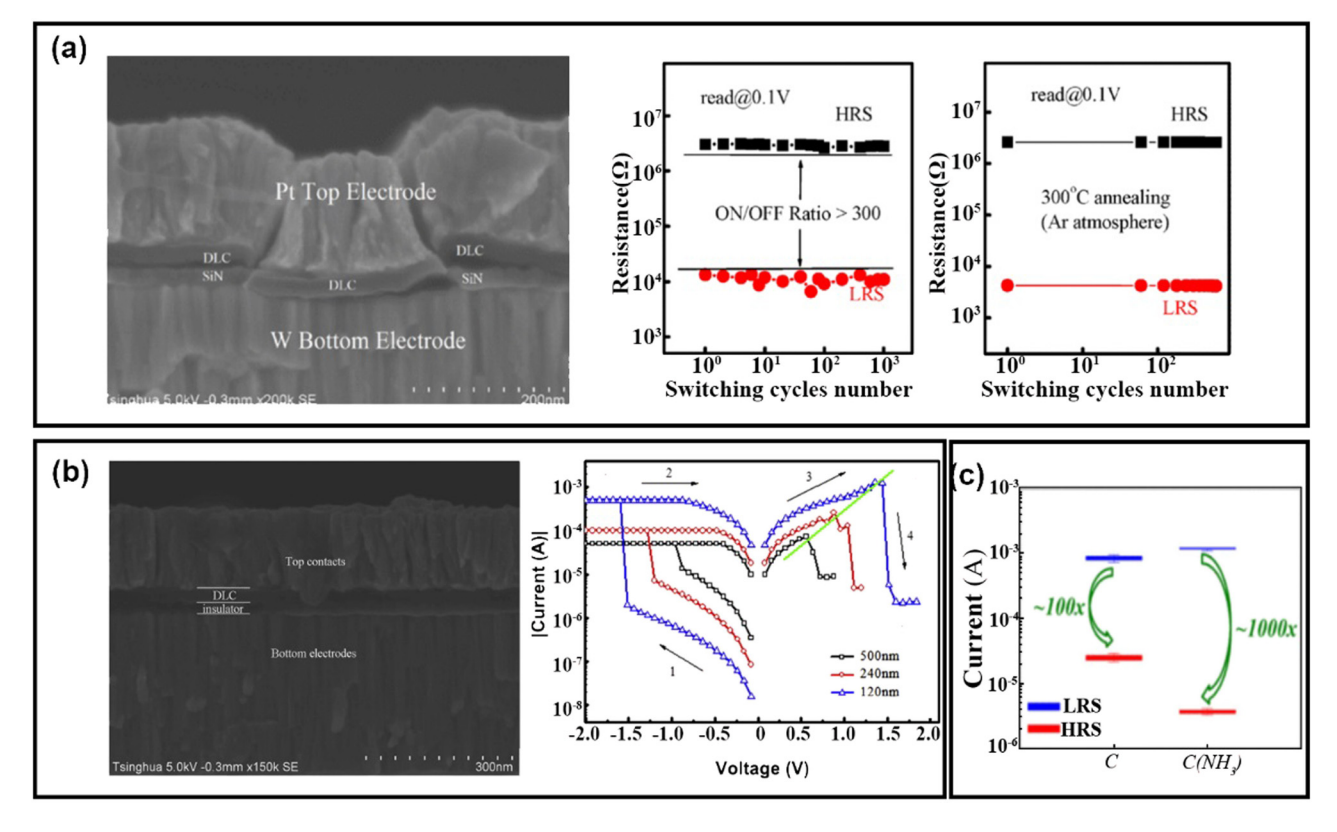


**Figure 7:** (a) Cross-sectional HRSEM image of an a-C memristor with W/a-C/Pt structure (left) and its HRS/LRS variation during endurance test (middle) and retention test (right), (b) cross-sectional HRSEM image of W/diamond-like carbon/Pt memristor (left) and its corresponding quasi-static I–V curves under different carbon thicknesses and CCs (right), (c) comparison of 100 cycles current between sputtering a-C with and without NH<sub>3</sub>. (a), (b), and (c) were reprinted with permission from [58,60,62], respectively.

Compared to conventional fabrication technology, such memristor induced ten times larger ON/OFF resistance ratio and much smaller leakage current during "forming" process. These advantageous features were ascribed to the replacement of some C-H bonds by C-NH<sub>2</sub> bonds in C(NH<sub>3</sub>) film. Therefore, the proportion of insulated sp<sup>3</sup> carbon in Pt/C(NH<sub>3</sub>)/TiN memristor was larger than that in Pt/a-C/TiN, giving rise to lower current at high-resistance level and larger memory window.

Table 2 summarizes the physical performances of various undoped a-C-based memristors.

#### 4.2 Doped a-C-based memristor

Doped a-C-based memristor can be classified into metaldoped a-C memristor [69-73], hydrogenated a-C (i.e., a-C:H) memristor [74-77], oxygenated a-C (i.e., a-C:O or a-CO<sub>x</sub>) memristor [78-83], and nitrogen-doped a-C (i.e., a-C:N) memristor [84-86]. The common metal dopants are Cobalt (Co) and Cu, and the doped a-C films can be prepared by either radio frequency reactive magnetron sputtering or direct current magnetron sputtering techniques [87]. One prototype was based on aluminum (Al)/a-C:Co/Fluorine-doped tin oxide (FTO) architecture that led to an ON/OFF ratio of 25 and retention time >10<sup>5</sup> s, as shown in Figure 8(a). Ohmic conduction and space charge limited current conduction were assumed to be responsible for threshold and sub-threshold regimes, respectively. The RS effect can be attributed to the formation/rupture of Co filaments in the film [69]. In contrast to inert electrodes, a-C:Co film combined with active electrodes also exhibited memristive characteristics, resulting in Au/a-C:Co/Au configuration [72], as illustrated in Figure 8(b). Such design enabled an ON/OFF ratio of >4, endurance of >200 cycles, and retention of >10<sup>5</sup> s. In addition to Co dopant, Cu element

was another common dopant that incorporated with a-C to secure CuC film. Accordingly, a Pt/CuC/Cu-based memristor was proposed, which exhibited bipolar switching behavior [70], as reflected in Figure 8(c). Differing from previous work, its RS mechanism was regarded as a tunneling between Cu filamentary channel and electrode through the solid electrolyte other than conduction through fully connected Cu filamentary channel. Table 3 summarizes the performance metrics of different metal-doped a-C memristors. As can be seen from Table 3, Co-doped a-C memristors have good time retention, so this material is able to maintain stable performance under different resistance states, which is suitable for long-term data storage. In addition, Co-doped a-C-based memristors usually have a fast switching speed, which is important for some high-performance applications. However, the preparation of Co-doped a-C-based amnesia may require complex processes that increase the manufacturing cost. Cu-doped a-C-based memristors typically exhibit a bistable resistance mechanism, allowing flexibility in non-volatile and volatile switching. However, their preparation, like Co-doping, requires more complex engineering treatments.

RS phenomenon was also observed on various nanoscale devices using a-C:H films. One representative structure, proposed by Zhuge *et al.* [75], was Cu/a-C:H/Pt memristor where a-C:H film was deposited by the linear ion beam deposition technique using  $C_2H_2$  as the precursor of hydrocarbon ions. Such RS behavior, as shown in Figure 8(d), resulted from the diffusion of the metal ions from active electrode, exhibiting ON/OFF ratio of >100 and retention time >10<sup>5</sup> s. The device, devised by Chen *et al.* [76], was analogous to Zhuge *et al.* [75], while replacing Cu electrode with inert Pt electrode. An intriguing finding was that in spite of the inert electrode, this device presented the bipolar switching characteristic. It was speculated that the negative bias can push hydrogen atoms away from the Pt electrode, which were absorbed by double bonds of sp<sup>2</sup> carbon. Such

Table 2: Performance comparison among different un-doped a-C memristors

Structure	$V_{\rm set}/V_{\rm reset}$ (V)	Endurance (cycles)	Retention (s)	Power density (W/µm²)	$R_{\rm On}/R_{\rm Off}$	Switching time (ns)	Ref.
Au/SLG/ta-C/Pt	_	>104	_	1.4 × 10 <sup>-5</sup>	10 <sup>5</sup>	4–50	[55]
Cu/a-C/Pt	1.5/-0.4	>1,000	>10 <sup>4</sup>	$3 \times 10^{-5}$	10 <sup>2</sup>	_	[56]
Pt/DLC/W	0.7/2.3	_	_	_	~8,000	_	[58]
Cu/a-C/Pt	_	_	_	_	100	_	[59]
W/DLC/Pt	_	>10 <sup>3</sup>	>6 × 10 <sup>3</sup>	_	>300	<50	[60]
Ag/TiOxNy/a-C/Pt	0.33/	>3 × 10 <sup>4</sup>	>10 <sup>4</sup>	_	30	_	[61]
Pt/C(NH3)/TiN	1/-1.4	>10 <sup>7</sup>	>10 <sup>4</sup>	_	1,000	_	[62]
Cu/a-C/Pt	0.1/-0.15	>10 <sup>4</sup> @300°C	10 <sup>8</sup>	$10^{-7}$	100	_	[63]
Cu/a-C/GMs/Ni	0.13-0.3/-0.13	>10 <sup>3</sup>	>10 <sup>4</sup> @85°C	_	100	_	[64]
Ag/a-C/CNT	5.4-7.5/-(5.4-7.5)	31	>10 <sup>6</sup>	0.48	40-200	_	[57]

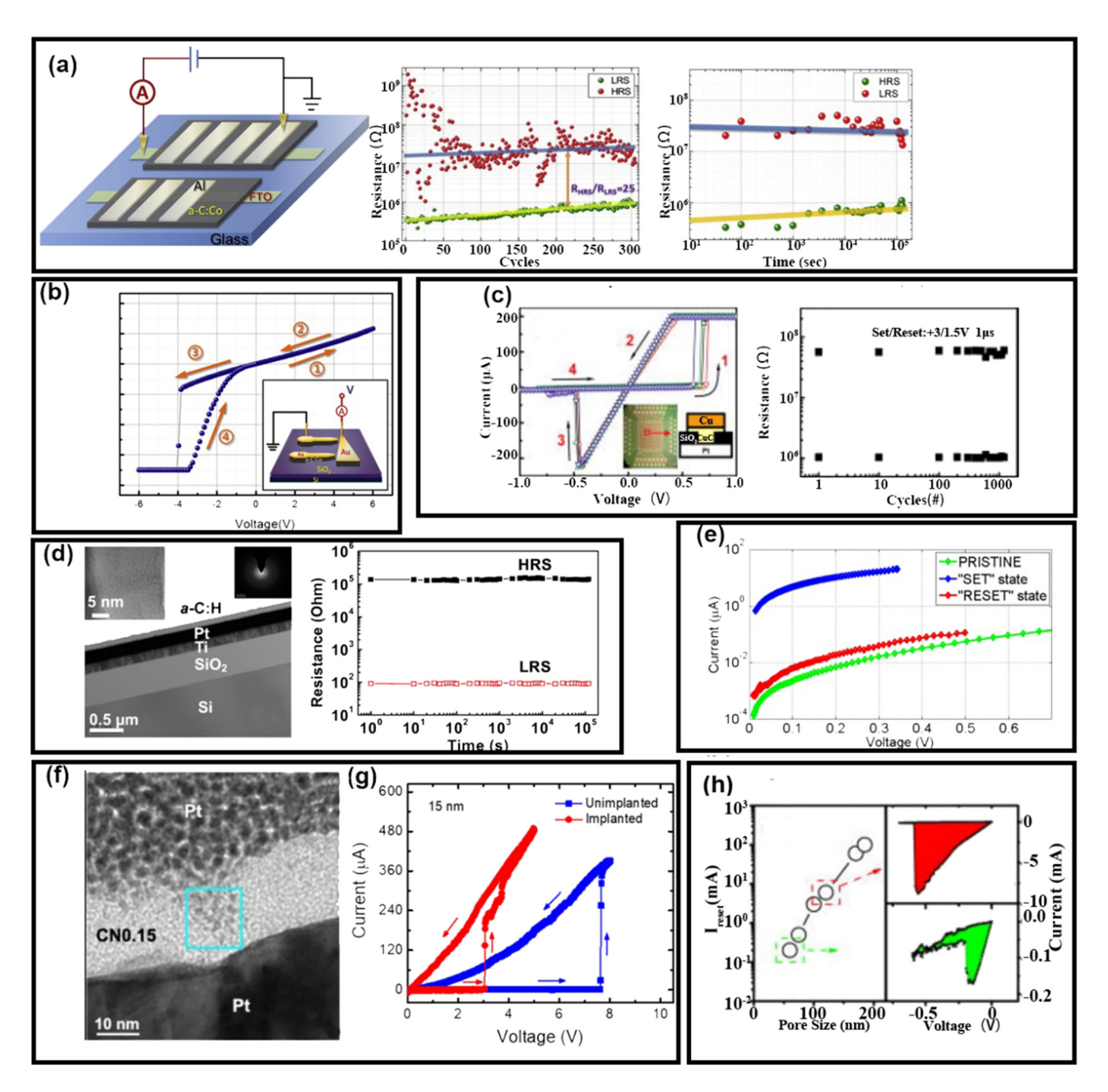


**Figure 8:** (a) Schematic of FTO/a-C:Co/Al memristor (left) and its HRS/LRS variation with respect to programming cycles (middle) and retention time (right), (b) typical I–V curve of Au/a-C:Co/Au memristor and its structural diagram, (c) measured I–V curve of Pt/CuC/Cu memristor (left) and its HRS/LRS distribution with respect to programming cycles (right). (d) Cross-sectional structure of a-C:H/Pt/Ti/SiO<sub>2</sub>/Si memristor (left) and its HRS/LRS states along with retention time, (e) measured I–V curves of TiN/a-C:H/Pt memristor for the "pristine," "SET" and "RESET" operations, (f) cross-sectional TEM image of the CN<sub>0.15</sub> thin film, (g) measured I–V curves for unimplanted and N<sub>2</sub>-implanted ta-C films at a thickness of 15 nm, (h) "RESET" current as a function of pore size (left), and corresponding I–V curves for pore diameter of 60 nm (top right) and 120 nm (bottom right). (a), (b), (c), (d), (e), (f), (g), and (h) were reprinted with permissions from [69,70,72,75,77,84–86], respectively.

hydrogenation process transformed the sp<sup>2</sup> CF into insulated sp<sup>3</sup> CF, inducing "RESET." Another design also adopted Cu/a-C:H/TiN configuration, while the polarity of the programming pulses was chosen such that the Cu did not diffuse into carbon, as reflected in Figure 8(e). A high ON/OFF

resistance ratio (>1,000), high switching speed (<30 ns), and non-destructive readout were observed [77].

In addition to a-C:H films, a-C:N films have also received considerable attention. A nanoporous nitrogen-doped a-C was deposited and a Pt/a-C:N/Cu architecture was subsequently

Table 3: Performance comparison among different metal-doped a-C memristors

Structure	V <sub>set</sub> /V <sub>reset</sub> (V)	Endurance (cycles)	Retention (s)	Power density (W/µm²)	R <sub>On</sub> /R <sub>Off</sub>	Switching time (ns)	Ref.
Cu-CuC/Pt	1.0/-1.1	>10 <sup>3</sup>	10⁴@85°C	_	>10 <sup>2</sup>	_	[70]
Pt/CuC/Pt	1.31-2.29/-2.38 to -1.32	_	_	_	_	_	[71]
Au/a-C:Co/Au	-4/-1.2	>200	>10 <sup>5</sup>	_	~4	_	[72]
Al/a-C:Co/FTO	_	_	>10 <sup>5</sup>	_	_	_	[69]
Pt/CuC/Pt	1.5/-1	_	_	_	10 <sup>2</sup>	_	[73]

fabricated [84], as illustrated in Figure 8(f). Switching voltage was reduced along with decreasing the nitrogen amount, and endurance of >1,000 cycles and retention of >80 days were attained. Unipolar switching trait was also found on a ta-C:N/ Pt/Ti/SiO<sub>2</sub>/Si structure when using doped diamond conductive tip as the top electrode [86], as illustrated in Figure 8(g). Unimplanted a-C films exhibited switching voltages between 7 and 10 V for ta-C films of thickness 15-40 nm, whereas nitrogen implanted films reduced the switching voltage by 60%. This was ascribed to the nitrogen implantation that benefited the size and number of sp<sup>2</sup> clusters. The memristor performances can be further improved on a Cu/nanoporous a-C:N/Pt configuration [85], resulting in Figure 8(h). Nanopore structure can facilitate Cu atoms to easily migrate into the films along the nanopores, leading to preformed CFs inside the film. Resulting preformed CFs can enhance the local electric field around CFs and mitigate the switching uniformity. In spite of this, the size and microgeometry of the preformed CFs were strongly affected by N2 partial pressure, thus impacting the switching fluctuation. Table 4 summarizes the various results on both a-C:H and a-C:N films.

As a-CO<sub>x</sub> can be prepared by a simple physical vapor deposition (PVD) technique at room temperature [87], a-CO<sub>x</sub>-based memristor has recently been under intensive research. One representative work was to produce a-CO<sub>x</sub> by PVD of a graphitic carbon target in oxygen [78], and the physical properties of a-CO<sub>x</sub> can be well tailored by

controlling the oxygen content. Accordingly, the deposited a-COx film was sandwiched between Pt top electrode and W bottom electrode to form metal-insulator-metal structure, as shown in Figure 9(a). Such design allowed for a switching speed of 10 ns, an endurance of >10<sup>4</sup>, and retention time of >10<sup>4</sup> s at 85°C. The "SET" operation was still dominated by conductive filaments mainly consisting of highly reduced a-COx, while the "RESET" operation was governed by partial dissolution of the CF with the help of the release of oxygen ions trapped in bottom electrode. Instead of inert electrode, an electrochemical metallization cell with Pt/a-CO<sub>x</sub>/Ag structure was fabricated. Such design provided both non-volatile and volatile switching characteristics [79], as illustrated in Figure 9(b). Non-volatile switching was readily ascribed to the formation and rupture of Ag ion filaments inside a-CO<sub>x</sub> film, whereas volatile switching was pertinent to the passivation of oxygen vacancies by thermally activated migration of oxygen ions. One promising strategy to improve a-CO<sub>x</sub>-based memristor was to stack an additional Cu layer on the original Pt/a-CO<sub>x</sub>/W frame [83], as shown in Figure 9(c). This interfacial layer gave rise to more Cu-O bonds and thus increased the sp<sup>2</sup> bond CFs. The advent of these Cu-O bonds can therefore suppress the random formation and rupture of sp<sup>2</sup> bond CFs, which can benefit the device reliability. Jin et al. [82] studied the bi-stable resistance mechanism of Pt/a-CO<sub>x</sub>/W memristor. The bi-stable resistance was likely to result

Table 4: Performance comparison among different a-C:H and a-C:N memristors

Structure	$V_{\rm set}/V_{\rm reset}$ (V)	Endurance (cycles)	Retention (s)	Power density (W/µm²)	R <sub>On</sub> /R <sub>Off</sub>	Switching time (ns)	Ref.
Metal/a-C:Pt	-1.2 to -0.8/0.6-2.2	>110	10 <sup>5</sup>	_	10 <sup>3</sup>	_	[75]
Pt/a-C:H/TiN	1.5/-	>10 <sup>7</sup>	10⁴@85°C	$9.4 \times 10^{-4} \sim 0.42$	100	_	[76]
TiN/a-C:H/Cu	_	_	>5.76 × 10 <sup>4</sup>	_	2,500	<30	[77]
CrN/a-C:H/Au	_	_	_	_	>100	_	[74]
Cu/DPCC/Pt	0.25/-1	>10 <sup>5</sup>	>10 <sup>5</sup> @85°C	$7.96 \times 10^{-7}$	10 <sup>2</sup>	<50	[85]
Cu/a-C:N/Pt	0.6/-0.5	1,000	>10 <sup>6</sup>	$7.64 \times 10^{-6}$	10 <sup>2</sup>	_	[84]
Conductive probe/a-C:N/Pt	_	_	_	_	_	5	[86]

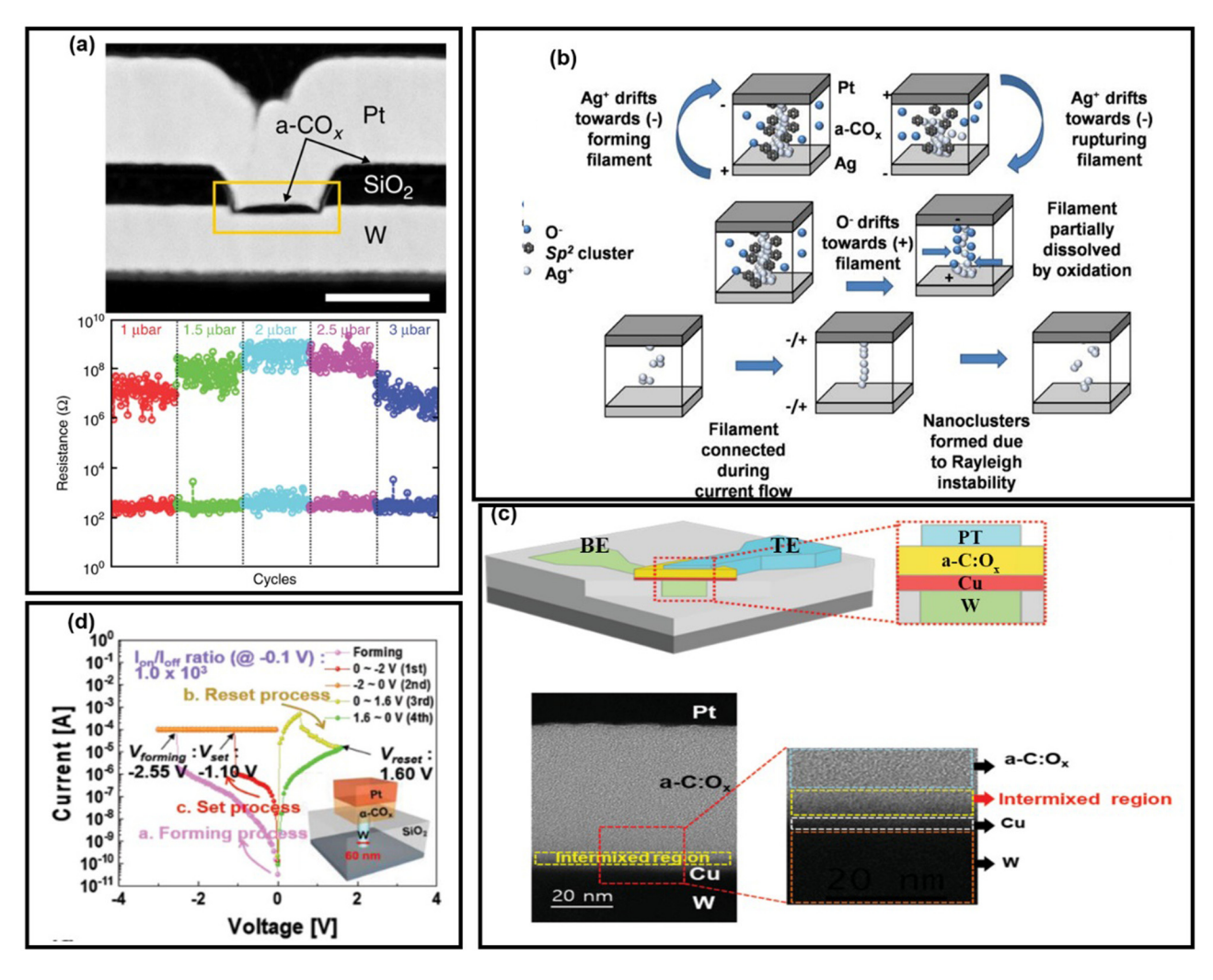


**Figure 9:** (a) HAADF-STEM image of an a-COx memristor (top) and its HRS/LRS states along with cycles under different oxygen pressure (bottom), (b) graphic interpretation of the non-volatile switching mechanism (top), the second forming process (middle), and the threshold switching mechanism (bottom) of Pt/a-CO<sub>x</sub>/Ag memristor, (c) schematic of W/Cu/a-CO<sub>x</sub>/Pt memristor, (d) typical I–V curves of a-COx memristor during forming, SET and RESET operations (left), and its cross-sectional TEM image (right). (a), (b), (c), and (d) are reprinted with permissions from [78–80,82], respectively.

from the  $O^{2-}$  distribution near the bottom W electrode, as demonstrated in Figure 9(d). Accordingly, the proportion of conductive C–C sp<sup>2</sup> covalent bond played a critical role in determining forming voltage and endurance. Performance comparison among different a-CO<sub>x</sub> memristors are detailed in Table 5.

## 5 a-C -based memristors for neuromorphic applications

It is well known that the most charming feature of memristor stems from its suitability for neuromorphic computing [88–92]. Neuromorphic computing is aiming to design both hardware and software computing elements that can operate in a manner similar to human brain. Today software computing elements require considerable computing source, usually accompanied with ultra-high energy consumption and relatively low computing efficiency. Hardware realization of neuromorphic computing is mainly based on complementary-metal-oxide-semiconductor transistors. Nevertheless, the integration density of the transistor-based device is approaching the limits of Moore's law [93], which can be hardly enhanced. Besides, the transistor-based devices still adopt the well-known von Neumann computational mode that data storage and processing functions are executed by memory and central processing unit, respectively. This mode is obviously against the biological mechanism of human brain where computation and storage are simultaneously

Table 5: Performance comparison among different a-C:H and a-C:N memristors

Structure	V <sub>set</sub> /V <sub>reset</sub> (V)	Endurance (cycles)	Retention (s)	Power density (W/µm²)	R <sub>On</sub> /R <sub>Off</sub>	Switching time (ns)	Ref.
Ag/a-COx/Pt	1/-1.65	>10 <sup>3</sup>	>10 <sup>5</sup>	_	5	<1.5 × 10 <sup>4</sup>	[79]
Pt/ta-C/a-Cox/Ag	0.2-0.7/-0.9	_	_	$3.18 \times 10^{-12}$	_	<50 × 10 <sup>6</sup>	[80]
Pt/a-COx/W	3.2/-2.5	_	_	_	_	_	[81]
Pt/a-COx/Cu/W	0.4/-0.6	>10 <sup>3</sup>	$HRS:5 \times 10^4 LRS:4 \times 10^4$	$5 \times 10^{-4}$	<10 <sup>2</sup>	30 (set) 20 (reset)	[83]
Pt/a-COx/SiO <sub>2</sub> /W	-1.10/1.6	>10 <sup>6</sup>	8.6 years	$3.1 \times 10^{-8}$	~10 <sup>3</sup>	85 (set) 75 (reset)	[82]
Pt/a-COx/SiO <sub>2</sub> /W	0.6/1.0	>104	>10 <sup>4</sup> @85°C	0.024	>10 <sup>2</sup>	10	[78]

processed in the same location. Under this circumstance, memristor that enables ultra-low power consumption, super-fast processing speed, and integration of data processing and computation presents the closest similarity to the key component of human brain, *i.e.*, biological synapse, as demonstrated in Figure 10. For the above reasons, the feasibility of using a-C-based memristor to mimic the biological response of human synapse has recently been under intensive research.

One promising design was to combine an additional aluminum oxide  $(AlO_x)$  layer with a- $CO_x$  memristor to form  $Cu/AlO_x/a-CO_x/TiN_xO_y/TiN$  configuration [94], as illustrated in Figure 11(a). The introduction of thin  $AlO_x$  layer can effectively control Cu migration, and enabled stable switching of >2,000 DC cycles, endurance of >1.5 ×  $10^9$  cycles, and switching speed of 100 ns. The device conductance experienced gradual increase when subjected to consecutive positive voltage, while continuously decreasing when undergoing consecutive negative voltage. Accordingly, a variety of conductance states, indicating the weight of the artificial synapse, can be obtained by varying the number of the applied pulses, demonstrating its long-term potentiation

(LTP) and long-term depression (LTD) functionalities. Meanwhile, Murdoch et al. [95] proposed a novel design based on amorphous zinc tin oxide (ZTO)/a-CO<sub>x</sub>/ta-C/Pt architecture. Such a transparent conducting ZTO electrode allowed the proposed device to effectively respond to both optical and electrical stimulations, thus triggering its optoelectronic function. As illustrated in Figure 11(b), paired-pulse facilitation (PPF), defined as an increased output current from two consecutive input stimuli, was induced on the proposed device using light pulses. The conductivity decay time, also called "forgetting" time, was also measured with respect to pulse intervals. The detected mapping presented an analogous trend to Ebbinghaus forgetting curves, accounting for the probability of short-term memory recall along with time [96]. Differing from previous work based on a-C films, a novel a-C memristor with carbon CFs based on carbon quantum dots (CQDs) was recently proposed [97], as illustrated in Figure 11(c). The designed memristor, i.e., palladium (Pa)/CQDs/gallium oxide (Ga2O3)/Pt, exhibited smaller programming power, longer retention, and better performance uniformity than the counterpart without CQDs. The

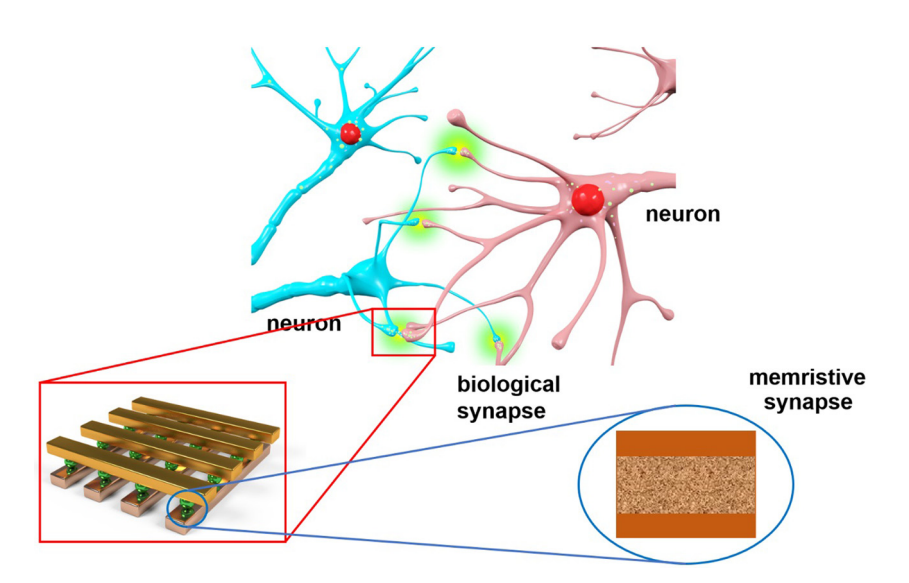
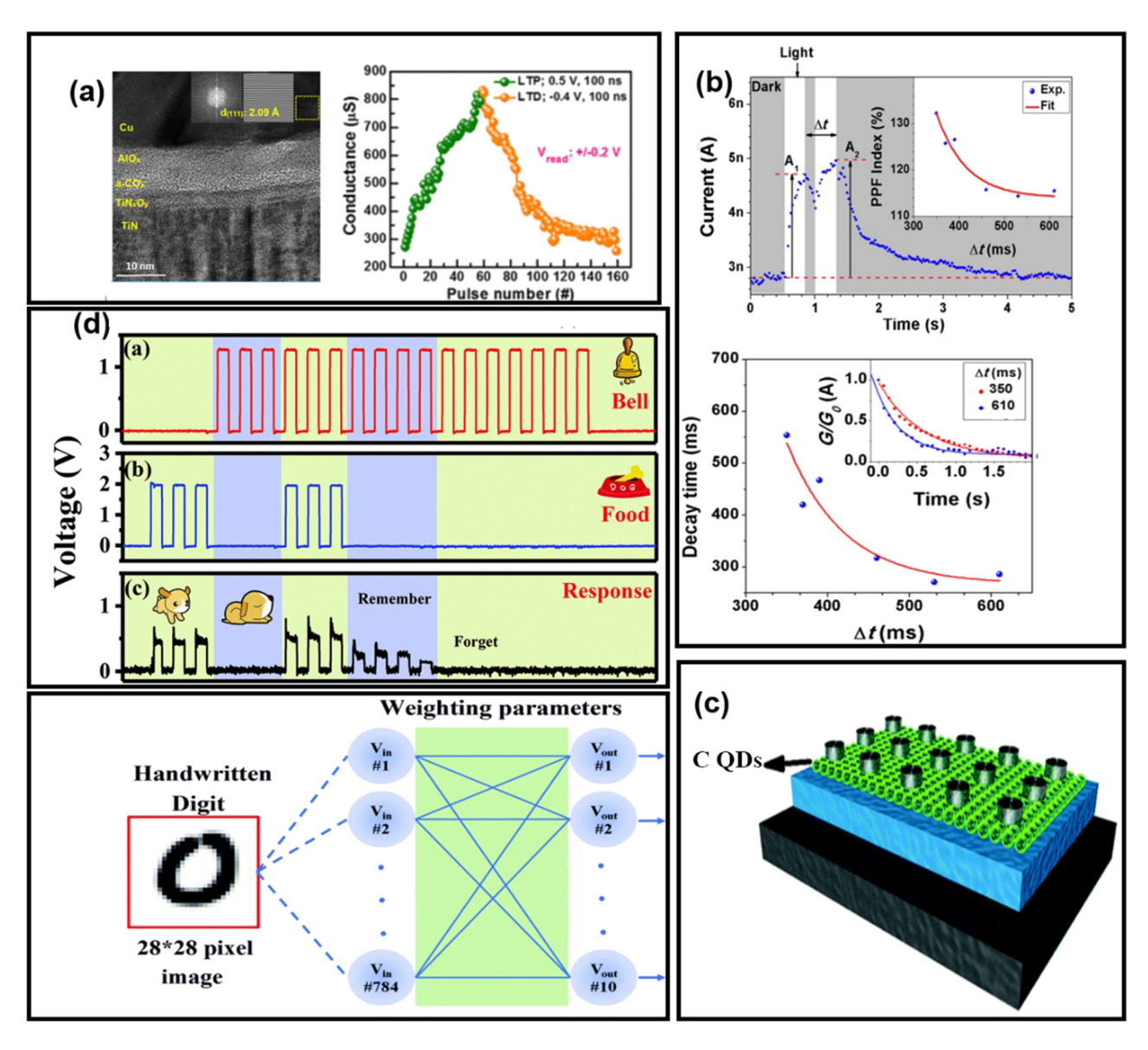


Figure 10: Illustration of the strategy of building memristor-based neural networks to imitate the biological neural networks.



**Figure 11:** (a) HAADF image of the  $Cu/AlO_x/a-CO_x/TiN_xO_y/TiN$  structure (left) and its LTP and LTD characteristics (right), (b) imitations of PPF (top) and STDP (bottom) mechanisms using the proposed light-gated a-C memristor, (c) schematic of CQD memristor device, and (d) experimental results of associative learning and forget relation (top) and designed neural network for hand-written digit recognition (bottom), realized by the CQD memristor device. (a) and (b) are reprinted with permissions from [94,95], respectively, while (c) and (d) are reprinted with permissions from [97].

fitting I–V curves indicated that the conduction behavior at HRS was governed by trap-assisted tunneling mechanism, whereas it was switched to ohmic contact at LRS due to the formation of carbon CFs. The proposed device can not only mimic the well-known LTP and LTD behaviors but also reproduce the important spike-timing-dependent plasticity (STDP) of the biological synapse such that the synaptic connection strength is determined by the relative timing of a particular neuron's output and input action potentials. Additionally, such devices also exhibited its ability for associative learning. To reproduce the associative learning behavior (i.e., Pavlovian conditioning), the "bell" and the "food" in

the top and middle rows of Figure 11(d), respectively, were defined as a neutral signal and an unconditioned stimulus, respectively, while "salivation" in the bottom row corresponded to the resulting reaction. When paired "bell" and "food" signals were applied to CMD, the initial resistance of CMD remained as HRS. Under such circumstance, only "food" signal led to unconditioned response, whereas only "bell" signal induced no reaction. The device was switched to LRS when both "bell" and "food" pulses were imposed on CMD simultaneously. During this process, these two signals were associated, indicating that only the "bell" signal allowed for the conditioned response. Most excitingly, hand written

digit recognition was achieved *via* a single-layer perceptron model comprised of the designed memristor, resulting in a recognition accuracy of 92.63%.

## 6 Technological challenges and future prospect

In principle, the memristive characteristic of a-C-based device strongly depends on its resistance switching between LRS and HRS, whereby a-C-based device falls into the category of ReRAMs. Accordingly, the performance metrics of a-C-based memristor are partly analogous to ReRAMs, as demonstrated in Table 6. When compared to its compatriots, the most attractive feature of a-C-based memristor perhaps arises from its excellent retention even at 250°C [98], thus rendering it practicable for automotive and harsh conditions [98]. Besides, a-C-based devices can be readily disposed and recycled, while independent of rare mineral extraction with low total energy production [99].

In spite of the above merits, it should be noted that a-C-based memristors are also facing some stringent challenges. In comparison with classic TMOs-based memristors, a-C-based memristor technologies are still at their youth stage. In contrast, TMOs-based technologies have been subjected to intensive research for more than 60 years, for which TMOs-based memristors have been consistently advanced since the debut of TiO<sub>2</sub>-based memristor in 2008 [100,101]. To date, the energy consumption, switching speed, endurance, and retention time of TMOs-based memristor have been incredibly improved, which obviously outpaces the state-of-the-art a-C-based technologies. According to Table 6, ON/OFF resistance ratio seems to lag far behind that of TMOs-based memristor. As presented above, this can be attractively mitigated by introducing an additional SLG layer between top electrode and a-C layer, which can reportedly circumvent the leakage currents owing to the low SLG density of states near the Dirac point [55]. This advanced technology brought ON/OFF resistance ratio to  $4 \times 10^5$  at 0.2 V. Endurance is another critical property over which TMOs-based memristor prevails a-C-based memristor. It can be however improved by using a-CO<sub>x</sub> film sandwiched by W top electrode and Pt bottom electrode [102]. This remarkably boomed the endurance to  $^{\sim}4 \times 10^4$  cycles. Additionally, using a-CO<sub>x</sub> allowed for "SET" and "RESET" speed of 40 and 4 ns, corresponding to programming energy of 2 and 1 pJ, respectively [102].

In terms of practical applications, it should be kept in mind that the systematic circuits in fact comprise a myriad of cells with inconsistent area and thickness, originating

Table 6: Performances comparison among various reported non-volatile RAMs

Structure	$V_{\rm set}/V_{\rm reset}$ (V)	Endurance (cycles)	Retention	Power (W)	Ron/Roff	Switching time (ns) Ref.	Ref.
Resistive RAM (RRAM)	0.13/-0.13@OHPs	$>10^{12}$ @Ta <sub>2</sub> O <sub>5</sub> -X/Ta <sub>2</sub> O <sub>5-X</sub>	10 years@150°C@Cu <sub>x</sub> Si <sub>y</sub> O	10 <sup>-4</sup> @HfO <sub>2</sub>	10 <sup>8</sup> @OHPs	10@Ta <sub>2</sub> O <sub>5</sub> /TaOX	[103–106]
PCRAM	1.5/-2@Ge2Sb2Te5	>10 <sup>12</sup> @ALD GST	10 years@70°C@GaSbGe	$2 \times 10^{-4}$ @Ge <sub>2</sub> Sb <sub>2</sub> Te <sub>5</sub>	$10^6$ @Ge <sub>2</sub> Sb <sub>2</sub> Te <sub>5</sub>	10@GeTe/Sb <sub>2</sub> Te <sub>3</sub>	[107–109]
FeRAM	1.8/-1.3@HfO <sub>2</sub> /ZrO <sub>2</sub>	$>10^{11}$ @Hf $_{0.5}$ Zr $_{0.5}$ O $_{2}$	>10 years@85°C@Hf <sub>0.5</sub> Zr <sub>0.5</sub> O <sub>2</sub>	$1.8 \times 10^{-4}$ @HfO <sub>2</sub> /ZrO <sub>2</sub>	>108@P(VDF-TrFE)	0.925@Hf <sub>0.5</sub> Zr <sub>0.5</sub> O <sub>2</sub>	[110–113]
MRAM	0.8/-0.5@MgO-CoFeB	>10 <sup>12</sup> @HfOx	10 years@MgO	1.56 × 10 <sup>-4</sup> @MgO-CoFeB	10 <sup>7</sup> @HfOx	10@HfOx	[114–116]
a-C Memristor	0.1/-0.15@a-C	>10 <sup>4</sup> @ta-C	8.6 years@a-COx	$4.8 \times 10^{-4}$ @a-C	$4 \times 10^{5}$ @ta-C	4(set)50(reset)@ta-C	[63,55,82,57]

from current immature fabrication technologies. This caused the so-called device-to-device variation [117,118]. Moreover, temporal stochasticity induced by the randomness in CF formations unwantedly gives rise to the cycleto-cycle variations [119,120]. Other reasons to cause cycle-tocycle variation may include the shape of the conductive filament, the oxygen vacancy distribution at and around the filament, and the changing location of the active filament between one cycle to the next. It was astonishing that both device-to-device and cycle-to-cycle variations of a-C-based memristors were rarely investigated at the time of writing. One viable scenario was to artificially form some more conductive dots or clusters inside a-C films [62], which can facilitate the growth of CFs along these pre-defined locations and thus overcome the randomness. Besides, depositing 2D materials such as graphene and MXene, on top of a-C films is likely to improve the cycle-to-cycle variations due to the fact that the CF can preferably grow along honeycombs of the 2D materials [121,122]. For potential applications of a-C-based memristors, multiple resistance states between HRS and LRS can be obtained by sophisticatedly tuning the size of the formed CFs. As a result, a-C-based memristor is capable of providing multilevel function, which can not only enhance the storage density but also provide synaptic and neuron-like mimics. This implied that a-C-based memristor can operate at the non-von-Neumann mode in which processing and storage are executed simultaneously [123,124]. In spite of its promising prospect for non-von-Neumann applications, a-C-based memristor was mainly devoted to the achievement of artificial synapse, while other attractive non-von-Neumann applications such as logic implementation and matrix computing are yet to be studied in detail. These two areas are very likely to become the future hotspots of a-C-based memristors.

#### 7 Conclusion

As one of the most important allotropes of carbon materials, a-C families exhibit distinct optoelectronic properties according to different dopants and proportion of bonding hybridization. Thanks to this, a-C families have been considered as one of the most promising memristive materials beyond Moore's law. However, a comprehensive review regarding the physical principles of different a-C-based memristors and their potential applications in the era of "non-von-Neumann" still remains vague. To address the above concerns, we here reviewed different types of a-C families whose memristive principles, architectures, modeling

methods, as well as merits and weakness, were elucidated in detail. Their promising applications for non-von-Neuman computing and storage, in association with some technical challenges were eventually discussed.

**Funding information:** This work was supported in part by the Science Foundation of Jiangsu Province (BK20211273, BZ2021031), in part by the National Natural Science Foundation of China under Grant 61964012, 52105369, 62371256, U22B2024, in part by the Nanjing university of posts and telecommunications under Grants NY220112, and in part by the Foundation of Jiangxi Science and Technology Department under Grant 20202ACBL21200.

**Author contributions:** All authors have accepted responsibility for the entire content of this manuscript and approved its submission.

**Conflict of interest:** The authors state no conflict of interest.

#### References

- [1] Kim K, Choi J-Y, Kim T, Cho S-H, Chung H-J. A role for graphene in silicon-based semiconductor devices. Nature. 2011;479:338–44.
- [2] Graham AP, Duesberg GS, Hoenlein W, Kreupl F, Liebau M, Martin R, et al. How do carbon nanotubes fit into the semiconductor roadmap. Appl Phys A. 2005;80:1141–51.
- [3] Wudl F. Fullerene materials. J Mater Chem. 2002;12:1959-63.
- [4] Shulaker MM, Hills G, Patil N, Wei H, Chen H-Y, Wong HSP, et al. Carbon nanotube computer. Nature. 2013;501:526–30.
- [5] Lee HC, Liu W-W, Chai S-P, Mohamed AR, Lai CW, Khe C-S, et al. Synthesis of single-layer graphene: a review of recent development. Procedia Chem. 2016;19:916–21.
- [6] Robertson J. Diamond-like amorphous carbon. Mater Sci Eng R. 2002;37(4–6):129–281.
- [7] Avouris P, Chen ZH, Perebeinos V. Carbon-based electronics. Nat Nanotechnol. 2007;2:605–15.
- [8] Giubileo F, Di Bartolomeo A, Lemmo L, Luongo G, Urban F. Field emission from carbon nanostructures. App Sci. 2018;8(4):526–44.
- [9] Yan M, Liu L, Chen L, Li N, Jiang Y, Xu Z, et al. Radiation resistance of carbon fiber-reinforced epoxy composites optimized synergistically by carbon nanotubes in interface area/matrix. Compos Part B. 2019;172(1):447–57.
- [10] Chua L. Memristor-The missing circuit element. IEEE Trans Circuit Theory. 1971;18(5):507–19.
- [11] Pan F, Gao S, Chen C, Song C, Zeng F. Recent progress in resistive random access memories: Materials, switching mechanisms, and performance. Mater Sci Eng R. 2014;83:1–59.
- [12] Mohammad B, Jaoude MA, Kumar V, Homouz DMA, Nahla HA, Qutayri MA, et al. State of the art of metal oxide memristor devices. Nanotechnol Rev. 2016;5(3):311–29.
- [13] Li Y, Wang Z, Midya R, Xia Q, Yang JJ. Review of memristor devices in neuromorphic computing: materials sciences and device challenges. J Phys D: Appl Phys. 2018;51(50):503002–12.

- [14] Amer S, Hasan MS, Rose GS. Analysis and modeling of electroforming in transition metal oxide-based memristors and its impact on crossbar array density. IEEE Electron Device Lett. 2017;39(1):19–22.
- [15] Pang Y, Gao B, Lin B, Qian H, Wu HQ. Memristors for hardware security applications. Adv Electron Mater. 2019;5(9):1800872–15.
- [16] Xu M, Mai X, Lin J, Zhang W, Li Y, He Y, et al. Recent advances on neuromorphic devices based on chalcogenide phase-change materials. Adv Electron Mater. 2020;30(50):2003419–10.
- [17] Zhang W, Mazzarello R, Wuttig M, Ma E. Designing crystallization in phase-change materials for universal memory and neuroinspired computing. Nat Rev Mater. 2019;4:150–68.
- [18] Chanthbouala A, Garcia V, Cherifi RO, Bouzehouane K, Fusil S, Moya X, et al. A ferroelecric memristor. Nat Mater. 2012;11:860–4.
- [19] Molinari A, Witte R, Neelisetty KK, Gorji S, Kubel C, Munch I, et al. Configurable resistive response in BaTiO<sub>3</sub> ferroelectric memristors via electron beam radiation. Adv Mater. 2020;32(12):1907541–6.
- [20] Mansueto M, Chavent A, Auffret S, Joumard I, Vila L, Sousa RC, et al. Spintronic memristors for neuromorphic circuits based on the angular variation of tunnel magnetoresistance. Nanoscale. 2021;13:11488–96.
- [21] Grollier J, Querlioz D, Camsari KY, Everschor-Sitte K, Fukami S, Stiles MD. Neuromorphic spintronics. Nat Electron. 2020;3:360–70.
- [22] Guo T, Sun B, Ranjan S, Jiao Y, Wei L, Zhou YN, et al. From memristive materials to neural networks. ACS Appl Mater Interfaces. 2020;12(49):54243–65.
- [23] Casiraghi C, Robertson J, Ferrari AC. Diamond-like carbon for data and beer storage. Mater Today. 2007;10(1–2):44–53.
- [24] Ferrari AC, Robertson J. Interpretation of Raman spectra of disordered and amorphous carbon. Phys Rev B. 2000;61:14095–5.
- [25] Ferrari AC, Robertson J. Resonant Raman spectroscopy of disordered, amorphous, and diamondlike carbon. Phys Rev B. 2001:64:075414–6.
- [26] Ferrari AC. Diamond-like carbon for magnetic storage disks. Surf Coat Technol. 2004:180–181:190–206.
- [27] Anders S, Diaz J, Ager JW, Lo R, Bogy DB. Thermal stability of amorphous hard carbon films produced by cathodic arc deposition. Appl Phys Lett. 1997;71(23):3367–9.
- [28] Fallon PJ, Veerasamy VS, Davis CA, Robertson J, Amaratunga GAJ, Miline WI, et al. Properties of filtered-ion-beam-deposited diamondlike carbon as a function of ion energy. Phys Rev B. 1993;48:4777–81.
- [29] Cooper NC, Fagan MS, Goringe CM, Marks NA, McKenzie DR. Surface structure and sputtering in amorphous carbon thin films: a tight-binding study of film deposition. J Phys: Condens Matter. 2002;14(4):723–9.
- [30] Tibrewala A, Peiner E, Bandorf R, Biehl S, Luthje H. Transport and optical properties of amorphous carbon and hydrogenated amorphous carbon films. Appl Surf Sci. 2006;252(15):5387–90.
- [31] Liu XY, Wang L, Tong Y. First-principles study of structural and opto-electronic characteristics of ultra-thin amorphous carbon films. Chin Phys B. 2022;31:016102–8.
- [32] Liu L, Lu F, Tian J, Xia S, Diao Y. Electronic and optical properties of amorphous carbon with different sp<sup>3</sup>/sp<sup>2</sup> hybridization ratio . Appl Phys B. 2019;125:366–10.
- [33] Morrison NA, Rodil SE, Ferrari AC, Robertson J, Milne WI. High rate deposition of ta-C:H using an electron cyclotron wave resonance plasma source. Thin Solid Films. 1999;337(1–2):71–3.
- [34] Yoon SF, Tan KH, Rusli, Ahn J. Modeling and analysis of hydrogenmethane plasma in electron cyclotron resonance chemical vapor deposition of diamond-like carbon. J Appl Phys. 2002;91(1):40–7.

- [35] Tamor MA, Vassell WC, Carduner KR. Atomic constraint in hydrogenated diamond-like carbon. Appl Phys Lett. 1991;58:592–4.
- [36] Koidl P, Wild Ch, Dischler B, Wagner J, Ramsteiner M. Plasma deposition, properties and structure of amorphous hydrogenated carbon films. Mater Sci Forum. 1990;52:41–70.
- [37] Weiler M, Lang K, Li E, Robertson J. Deposition of tetrahedral hydrogenated amorphous carbon using a novel electron cyclotron wave resonance reactor. Appl Phys Lett. 1998;72(11):1314–6.
- [38] Weiler M, Sattel S, Giessen T, Jung K, Ehrhardt H, Veerasamy VS, et al. Preparation and properties of highly tetrahedral hydrogenated amorphous carbon. Phys Rev B. 1996;53(11):1594–6.
- [39] Jimenez I, Gago R, Albella JM, Caceres D, Vergara I. Spectroscopy of Π bonding in hard graphitic carbon nitride films: Superstructure of basal planes and hardening mechanisms. Phys Rev B. 2000;62(7):4261–6.
- [40] Gammon WJ, Malyarenko DI, Kraft O, Hoatson GL, Reilly AC, Holloway BC. Hard and elastic amorphous carbon nitride thin films studied by <sup>13</sup>C nuclear magnetic resonance spectroscopy . Phys Rev B. 2002;66(15):153402–10.
- [41] Ferrari AC, Rodil SE, Robertson J. Interpretation of infrared and Raman spectra of amorphous carbon nitrides. Phys Rev B. 2003;67(15):155306–10.
- [42] Rodil SE, Milne WI, Robertson J, Brown LM. Maximized sp<sup>3</sup> bonding in carbon nitride phases . Appl Phys Lett. 2000;77:1458–60.
- [43] Hammer P, Victoria NM, Alvarez F. Electronic structure of hydrogenated carbon nitride films. J Vac Sci Technol A. 1998;16:2941–9.
- [44] Silva SRP, Robertson J, Amaratunga GAJ, Rafferty B, Brown LM, Schwan J, et al. Nitrogen modification of hydrogenated amorphous carbon films. J Appl Phys. 1997;81:2626–34.
- [45] Hellgren N, Johansson MP, Broitman E, Hultman L, Sundgren J-E. Role of nitrogen in the formation of hard and elastic CN<sub>x</sub> thin films by reactive magnetron sputtering . Phys Rev B. 1999:59(7):5162–7.
- [46] Kreupl F, Bruchhaus R, Majewski P, Philipp JB, Symanczyk R, Happ T, et al. Carbon-based resistive memory. 2008 IEDM; 2009. p. 1–4.
- [47] Sebastian A, Pauza A, Rossel C, Shelby RM, Rodriguez AF, Pozidis H, et al. Resistance switching at the nanometer scale in amorphous carbon. N J Phys. 2011;13:013020–12.
- [48] Wang L, Liu Z-G, Yang C-H, Wen J, Xiong B-S. Scanning probe memory with patterned amorphous carbon layer. Appl Phys Express. 2019;12:075012–5.
- [49] Bachmann TA, Alexeev AM, Koelmans WW, Zipoli F, Ott AK, Dou C, et al. Temperature evolution in nanoscale carbon-based memory devices due to local Joule heating. IEEE Trans Nanotechnol. 2017;16(5):806–11.
- [50] Qin SJ, Zhang JY, Fu D, Xie D, Wang Y, Qian H, et al. A physics/ circuit-based switching model for carbon-based resistive memory with sp<sup>2</sup>/sp<sup>3</sup> cluster conversion. Nanoscale. 2012;4:6658–63.
- [51] Ou Q-F, Wang L, Xiong B-S. Modeling electrical switching behavior of carbon resistive memory. IEEE Access. 2020;8:8735–42.
- [52] Gerstner EG, McKenzie DR. Nonvolatile memory effects in nitrogen doped tetrahedral amorphous carbon thin films. J Appl Phys. 1998;84:5647.
- [53] Raeber TJ, Zhao ZC, Murdoch BJ, McKenzie DR, McCulloch DG andPartridge JG. Resistive switching and transport characteristics of an all-carbon memristor. Carbon. 2018;136:280–5.
- [54] Liu Z-C, Wang L. Carbon resistive probe memory designed for ultra-high storage density. Nanotechnology. 2020;31:385204–10.

- [55] Ott AK, Dou C, Sassi U, Goykhman I, Yoon D, Wu J, et al. Tetrahedral amorphous carbon resistive memories with graphene-based electrodes. 2D Mater. 2018;5:045028–10.
- [56] Zhao XN, Xu HY, Wang ZQ, Xu Z, Zhang C, Wang G, et al. Sp<sup>2</sup>-clustering induced improvement of resistive switching uniformity in Cu/amorphous carbon/Pt electrochemical metallization memory. J Mater Chem C. 2017;5:5420–5.
- [57] Chai Y, Wu Y, Takei K, Chen H-Y, Yu SM, Chan PCH, et al. Nanoscale bipolar and complementary resistive switching memory based on amorphous carbon. IEEE Trans Electron Devices. 2011;58(11):3933–9.
- [58] Xu J, Xie D, Feng T, Zhang C, Zhang X, Peng P, et al. Scaling-down characteristics of nanoscale diamond-like carbon based resistive switching memories. Carbon. 2014;75:255–61.
- [59] Zhao X, Xu H, Wang Z, Zhang L, Ma J, Liu YC. Nonvolatile/volatile behaviors and quantized conductance observed in resistive switching memory based on amorphous carbon. Carbon. 2015;91:38–44.
- [60] Fu D, Xie D, Feng T, Zhang C, Niu J, Qian H, et al. Unipolar resistive switching properties of diamondlike carbon-based RRAM devices. IEEE Electron Device Lett. 2011;32(6):803–5.
- [61] Zhao X, Wang Z, Xu H, Xie Y, Ma H, Ma J, et al. Reliability improvement of amorphous carbon based resistive switching memory by inserting nanoporous layer. IEEE Electron Device Lett. 2016;37(11):1430–3.
- [62] Chen W-C, Tsai T-M, Chang K-C, Chen H-L, Shih C-C, Yang C-C, et al. Influence of ammonia on amorphous carbon resistive random access memory. IEEE Electron Device Lett. 2017;38(4):453–6.
- [63] Zhao YP, Li Y. Nano-graphite clusters regulation for reliability improvement of amorphous carbon based RRAM. Phys Status Solidi A. 2019;216(20):1900278.
- [64] Ding W, Tao Y, Li X, Lin Y, Wang Z, Xu H, et al. Graphite microislands prepared for reliability improvement of amorphous carbon based resistive switching memory. Phys Status Solidi RRL. 2018;12(10):1800285–8.
- [65] Yanagida T, Nagashima K, Oka K, Kanai M, Klamchuen A, Park BH, et al. Scaling effect on unipolar and bipolar resistive switching of metal oxides. Sci Rep. 2013;3:1657–12.
- [66] Praveen P, Priya Rose T, Saji KJ. Top electrode dependent resistive switching in M/ZnO/ITO memristors, M = Al, ITO, Cu, and Au. Microelectron J. 2022;121:105388–6.
- [67] Yang Y, Gao P, Li L, Pan X, Tappertzhofen S, Choi S, et al. Electrochemical dynamics of nanoscale metallic inclusions in dielectrics. Nat Commun. 2014;5:4232.
- [68] Carey JD, Silva SRP. Conditioning of hydrogenated amorphous carbon thin films for field emission via current stressing. Appl Phys Lett. 2001;78:347.
- [69] Zhang S, Zhou J, Zhang D, Ren B, Wang L, Huang J, et al. Nonvolatile resistive switching in Co doped amorphous carbon film. Vacuum. 2016;125:189–91.
- [70] Pyun M, Choi H, Park J-B, Lee D, Hasan M, Dong R, et al. Electrical and reliability characteristics of copper-doped carbon (CuC) based resistive switching devices for nonvolatile memory applications. Appl Phys Lett. 2008;93:212907–4.
- [71] Kim D-I, Yoon J, Park J-B, Hwang H, Kim YM, Kwon SH, et al. Nonlinear current-voltage behavior of the isolated resistive switching filamentary channels in CuC nanolayer. Appl Phys Lett. 2011;98:152107–3.
- [72] Zhang D, Li TR, Zhou JW, Jiang YC, Ren B, Huang J, et al. Asymmetric resistive switching behaviour in a Au/a-C:Co/Au planar structure. Microelectron Reliab. 2018;87:52–6.

- [73] Choi H, Pyun M, Kim T-W, Hasan M, Dong R, Lee J, et al. Nanoscale resistive switching of a copper-carbon-mixed layer for nonvolatile memory applications. IEEE Electron Device Lett. 2009;30(3):302–4.
- [74] Khan RUA, Silva SRP. Switching phenomena in boron-implanted amorphous carbon films. Diam Relat Mater. 2001;10(3–7):1036–9.
- [75] Zhuge F, Dai W, He CL, Wang AY, Liu YW, Li M, et al. Nonvolatile resistive switching memory based on amorphous carbon. Appl Phys Lett. 2010;96:163505–3.
- [76] Chen Y-J, Chen H-L, Young T-F, Chang T-C, Tsai T-M, Chang K-C, et al. Hydrogen induced redox mechanism in amorphous carbon resistive random access memory. Nanoscale Res Lett. 2014;9:52–6.
- [77] Dellmann L, Sebastian A, Jonnalagadda P, Santini CA, Koelmans WW, Rossel C, et al. Nonvolatile resistive memory devices based on hydrogenated amorphous carbon. 2014 Proceedings of the European Solid-State Device Research Conference; 2014. p. 1–4.
- [78] Santini CA, Sebastian A, Marchiori C, Jonnalagadda VP, Dellmann L, Koelmans WW, et al. Oxygenated amorphous carbon for resistive memory applications. Nat Commun. 2015;6:8600–8.
- [79] Murdoch BJ, Raeber TJ, Barlow AJ, McCulloch DG, Partidge JG. Non-volatile and volatile memory behaviour in oxygenated amorphous carbon electrochemical metallization devices. Appl Phys Lett. 2018;112:8242903–5.
- [80] Murdoch BJ, Raeber TJ, Zhao ZC, McKenzie DR, McCulloch DG, Partridge JG. Temperature sensitivity and short-term memory in electroforming-free low power carbon memristor. Appl Phys Lett. 2019;114:163504–5.
- [81] Bachmann TA, Koelmans WW, Jonnalagadda VP, Le Gallo M, Santini CA, Sebastian A, et al. Memristive effects in oxygenated amorphous carbon nanodevices. Nanotechnology. 2018;29(3):035201–5.
- [82] Jin S-M, Kim H-J, Woo D-S, Jung S-M, Kim D-E, Shim T-H, et al. Bistable resistance generation mechanism for oxygenated amorphous carbon-based resistive random-access memory. Adv Electron Mater. 2022;8:2101083–12.
- [83] Hyeon DS, Jang G, Min S, Hong JP. Highly stable forming-free bipolar resistive switching in Cu layer stacked amorphous carbon oxide: transition between C-C bonding complexes. Adv Electron Mater. 2022;8:2100660–9.
- [84] Chen H, Zhuge F, Fu B, Li J, Wang J, Wang W, et al. Forming-free resistive switching in a nanoporous nitrogen-doped carbon thin film with ready-made metal nanofilaments. Carbon. 2014;76:459–63.
- [85] Tao Y, Li X, Wang Z, Xu H, Ding W, Ma J, et al. Improved resistive switching reliability by using dual-layer nanoporous carbon structure. Appl Phys Lett. 2017;111:183504–5.
- [86] Nagareddy VK, Ott AK, Dou C, Tsvetkova T, Sandulov M, Craciun MF, et al. The effect of nitrogen implantation on resistive switching of tetrahedral amorphous carbon films. Diam Relat Mater. 2018;87:90–8.
- [87] Hui F, Grustan-Gutierrez E, Long S, Liu Q, Ott AK, Ferrari AC, et al. Graphene and related materials for resistive random access memories. Adv Electron Mater. 2017;3(8):1600195–32.
- [88] Cao J, Zhang X, Cheng H, Qiu J, Liu X, Wang M, et al. Emerging dynamic memristors for neuromorphic reservoir computing. Nanoscale. 2022;14:289–98.
- [89] Indiveri G, Linares-Barranco B, Legenstein R, Deligeorgis G, Prodromakis T. Integration of nanoscale memristor synapses in

- neuromorphic computing architectures. Nanotechnology. 2013;24(38):2384010.
- [90] Sung C, Hwang H, Yoo IK. Perspective: a review on memristive hardware for neuromorphic computation. J Appl Phys. 2018;124:151903–6.
- [91] Sokolov AS, Abbas H, Abbas Y, Choi C. Towards engineering in memristors for emerging memory and neuromorphic computing: A review. J Semicond. 2021;42(1):013101–6.
- [92] Chen W, Song L, Wang S, Zhang Z, Wang G, Hu G, et al. Essential characteristics of memristors for neuromorphic computing. Adv Electron Mater. 2023;9(2):2200833–12.
- [93] Cavin RK, Lugli P, Zhirnov VV. Science and engineering beyond Moore's law. Proc IEEE. 2012;100:1720–49.
- [94] Ginnaram S, Qiu JT, Maikap S. Controlling Cu migration on resistive switching, artificial synapse, and glucose/saliva detection by using an optimized AlO<sub>x</sub> interfacial layer in a-CO<sub>x</sub>-based conductive bridge random access memory. ACS Omega. 2020;5:7032–43.
- [95] Murdoch BJ, Raeber TJ, Zhao ZC, Barlow AJ, McKenzie DR, McCulloch DG, et al. Light-gated amorphous carbon memristors with indium-free transparent electrodes. Carbon. 2019;152:59–65.
- [96] Murre JMJ, Dros J. Replication and analysis of Ebbinghaus' forgetting curve. PLoS One. 2015;10:e0120644–12.
- [97] Pei Y, Zhou Z, Chen A, Chen J, Yan X. A carbon-based memristors design for associative learning activities and neuromorphic computing. Nanoscale. 2020;12:13531–39.
- [98] Kreupl F. Carbon memory assessment, white paper for the ITRS meeting on emerging research devices (ERD) in Albuquerque, New Mexico, on August 25–26; 2014.
- [99] CareRAMM public summary. http://emps.exeter.ac.uk/media/ universityofexeter/emps/careramm/D4.4\_Public\_summary\_of\_ project\_results\_from\_the\_third\_year\_of\_the\_project.pdf. (Accessed July 2023).
- [100] Strukov DB, Snider GS, Stewart DR, Williams RS. The missing memristor found. Nature. 2008:453:80–3.
- [101] Yang JJ, Pickett MD, Li X, Ohlberg DAA, Stewart DR, Williams RS. Memristive switching mechanism for metal/oxide/metal nanodevices. Nat Nanotechnol. 2008;3(7):429–33.
- [102] Koelmans WW, Bachmann T, Zipoli F, Ott AK, Dou C, Ferrari AC, et al. Carbon-based resistive memories. IEEE (IMW). 2016;1–4.
- [103] Zhang C, Li Y, Ma C, Zhang Q. Recent progress of organic-inorganic hybrid perovskites in RRAM, artificial synapse, and logic operation. Small Sci. 2021;2:210086–18.
- [104] Wang M, Luo WJ, Wang YL, Yang LM, Zhu W, Zhou P, et al. "A novel Cu(x)Si(y)O resistive memory in logic technology with excellent data retention and resistance distribution for embedded applications. IEEE. 2010;89–90.
- [105] Woo J, Moon K, Song J, Kwak SLM, Park J, Hwang H. Improved synaptic behavior under identical pulses using AlO<sub>x</sub>/HfO<sub>2</sub> bilayer RRAM array for neuromorphic systems. IEEE Electron Device Lett. 2016;37:994–7.
- [106] Wang H, Yan X. Overview of resistive random access memory (RRAM): materials, filament mechanisms, performance optimization, and prospects. Phys Status Solidi RRL. 2019;13(9):190073–10.
- [107] Raeis-Hosseini N, Rho J. Dual-functional nanoscale devices using phase-change materials: a reconfigurable perfrect absorber with nonvolatile resistance-change memory characteristics. App Sci. 2019:9:564–74.
- [108] Fong SW, Neumann CM, Wong HSP. Phase-change memory Towards a storage-class memory. IEEE Trans ElectrDevices. 2017;64(11):4374–85.

- [109] Cheng HY, Chien WC, BrightSky M, Ho YH, Zhu Y, Ray A, et al. Novel fast-switching and high-data retention phase-change memory based on new Ga-Sb-Ge material. Proceedings of 2019 IEDM; 2015. p. 3–5.
- [110] Tang L, Maruyama H, Han T, Nino JC, Chen Y, Zhang D. Resistive switching in atomic layer deposited HfO<sub>2</sub>/ZrO<sub>2</sub> nanolayer stacks. Appl Surf Sci. 2020;515:146015.
- [111] Okuno J, Kunihiro T, Konishi K, Maemura H, Shuto Y, Sugaya F, et al. SoC compatible 1T1C FeRAM memory array based on ferroelectric Hf0.5Zr0.5O2. 2020 IEEE Symposium on VLSI Technology; 2020. p. 1–2.
- [112] Zhao Q, Wang H, Ni Z, Liu J, Zhen Y, Zhang X, et al. Organic ferroelectric-based 1T1T random access memory cell employing a common dielectric layer overcoming the half-selection problem. Adv Mater. 2017;29:1701907.
- [113] Lyu X, Si M, Shrestha PR, Cheung KP, Ye PD. First direct measurement of sub-nanosecond polarization switching in ferroelectric hafnium zirconium oxide. Proceedings of 2019 IEDM; 2019. p. 1–4.
- [114] Wang DY, Hsin YC, Lee KY, Chen GL, Yang SY, Lee HH, et al. Hardware implementation of physically unclonable function (PUF) in perpendicular STT MRAM. Proceedings of 2017 VLSI-TSA; 2017. p. 1–2.
- [115] Miura S, Nishioka K, Naganuma H, Nguyen TA, Honjo H, Ikeda S, et al. Scalability of Quad Interface p-MTJ for 1X nm STT-MRAM With 10-ns Low Power Write Operation, 10 Years Retention and Endurance > 1011. IEEE Trans ElectrDevices. 2020;67:5368–73.
- [116] Yang H, Hao X, Wang Z, Malmhall R, Gan H, Satoh K, et al. Threshold switching selector and 1S1R integration development for 3D cross-point STT-MRAM. Proceedings of 2017 IEDM; 2017. p. 38–1.
- [117] Lee J-H, Lim D-H, Jeong H, Ma H, Shi LP. Exploring cycle-to-cycle and device-to-device variation tolerance in MLC storage-based neural network training. IEEE Trans Electron Devices. 2019;66(5):2172–8.
- [118] Pan W-Q, Chen J, Kuang R, Li Y, He Y-H, Feng G-R, et al. Strategies to improve the accuracy of memristor-based convolutional neural networks. IEEE Trans Electron Devices. 2020;67(3):895–901.
- [119] Fu JY, Liao ZH, Wang JH. Level scaling and pulse regulating to mitigate the impact of the cycle-to-cycle variation in memristorbased edge AI system. IEEE Trans Electron Devices. 2022;69(4):1752–62.
- [120] Dalgaty T, Castellani N, Turck C, Harabi K-E, Querlioz D, Vianello E. In situ learning using intrinsic memristor variability via Markov chain Monte Carlo sampling. Nat Electron. 2021;4:151–61.
- [121] Chen Y, Wang Y, Luo Y, Liu X, Wang Y, Gao F, et al. Realization of artificial neuron using MXene bi-directional threshold switching memristors. IEEE Electron Device Lett. 2019;40:1686–9.
- [122] Lian X, Shen X, Zhang M, Xu J, Gao F, Wan X, et al. Resistance switching characteristics and mechanisms of MXene/SiO<sub>2</sub> structure-based memristor . Appl Phys Lett. 2019;115:063501–4.
- [123] Ismail M, Mahata C, Kim S. Forming-free Pt/Al<sub>2</sub>O<sub>3</sub>/HfO<sub>2</sub>/HfAlO<sub>x</sub>/ TiN memristor with controllable multilevel resistive switching and neuromorphic characteristics for artificial synapse . J Alloy Compd. 2022;892:162141–8.
- [124] Wang TY, Meng JL, Li QX, Chen L, Zhu H, Sun Q, et al. Forming-free flexible memristor with multilevel storage for neuromorphic computing by full PVD technique. J Mater Sci Technol. 2021;60:21–6.